Discovery of pan-ErbB inhibitors protecting from SARS-CoV-2 replication, inflammation, and lung injury by a drug repurposing screen

Sirle Saul [1, 12], Marwah Karim[1, 12], Pei-Tzu Huang[1, 13], Luca Ghita[1,13], Winston Chiu[2], Sathish Kumar[1], Nishank Bhalla[3], Pieter Leyssen[2], Courtney A. Cohen[4], Kathleen Huie[4], Courtney Tindle[5, 6], Mamdouh Sibai [7], Benjamin A. Pinsky[7, 1], Soumita Das[6, 8], Pradipta Ghosh[5, 6, 9], John M. Dye[4], David E. Solow-Cordero[10], Jing Jin[11], Dirk Jochmans[2], Johan Neyts[2], Aarthi Narayanan[3], Steven De Jonghe[2], and Shirit Einav[1, *]

[1]Department of Medicine, Division of Infectious Diseases and Geographic Medicine, and Department of Microbiology and Immunology, Stanford University, CA, USA
[2] KU Leuven, Department of Microbiology, Immunology and Transplantation, Rega Institute for Medical Research, Laboratory of Virology and Chemotherapy, Belgium
[3]National Center for Biodefence and Infectious Disease, Biomedical Research Laboratory, School of Systems Biology, George Mason University, Manassas, VA, USA.
[4]US Army Medical Research Institute of Infectious Diseases, Viral Immunology Branch, Fort Detrick, Maryland
[5] Department of Cellular and Molecular Medicine, University of California San Diego
[6] HUMANOID CoRE, University of California San Diego.
[7]Department of Pathology, Stanford University School of Medicine, Stanford, California, USA
[8]Department of Pathology, University of California San Diego
[9]Department of Medicine, University of California San Diego
[10]High-Throughput Bioscience Center, Department of Chemical and Systems Biology, Stanford University, CA
[11] Vitalant Research Institute, San Francisco, CA, USA

* Corresponding author and lead contact: seinav@stanford.edu

[12]These authors contributed equally
[13]These authors also contributed equally

Abstract

Effective therapies are needed to combat emerging viruses. Seventeen candidates that rescue cells from SARS-CoV-2-induced lethality and target diverse functions emerged in a screen of 4,413 compounds. Among the hits was lapatinib, an approved inhibitor of the ErbB family of receptor tyrosine kinases. Lapatinib and other pan-ErbB inhibitors suppress replication of SARS-CoV-2 and unrelated viruses with a high barrier to resistance. ErbB4, but not lapatinib's cancer targets ErbB1 and ErbB2, is required for SARS-CoV-2 entry and encephalitis alphavirus infection and is a molecular target mediating lapatinib's antiviral effect. In human lung organoids, lapatinib protects from SARS-CoV-2-induced activation of pathways implicated in non-infectious acute lung injury and fibrosis downstream of ErbBs (p38-MAPK, MEK/ERK, and AKT/mTOR), pro-inflammatory cytokine production, and epithelial barrier injury. These findings reveal regulation of viral infection, inflammation, and lung injury via ErbBs and propose approved candidates to counteract these effects with implications for pandemic coronaviruses and unrelated viruses.

Introduction

Severe acute respiratory syndrome coronavirus-2 (SARS-CoV-2) has spread globally, resulting in the Coronavirus Disease 2019 (COVID-19) pandemic. While largely asymptomatic or mild, in 3-21% of symptomatic patients, COVID-19 progresses to acute lung injury (ALI) and acute respiratory distress syndrome (ARDS) associated with a 5-20% 28-day death rate in face of standard of care[1-3]. Survivors of severe COVID-19 are also at risk of developing lung fibrosis[4].

The development of countermeasures that reduce COVID-19 morbidity and mortality via off-label use of existing drugs has been an area of much global research. Unbiased screens have discovered repurposing drug candidates for the treatment of COVID-19[5,6,7,8], several of which are still studied clinically. Nevertheless, to date the reported clinical benefit in reducing complication and mortality rates has been overall limited[9]. Moreover, no single agent capable of suppressing viral infection, inflammation and tissue injury has been identified. There is thus an urgent need for more effective approaches to prevent the acute and long-term complications associated with COVID-19 and ideally provide readiness for future outbreaks.

To address these gaps, we conducted a high-throughput screen of existing compounds for agents that rescue mammalian cells from SARS-CoV-2-induced lethality. Among the promising hits were inhibitors of members of the ErbB family of receptor tyrosine kinases, including lapatinib, an approved anticancer drug. Here, we reveal regulation of SARS-CoV-2 infection and pathogenesis via ErbBs and characterize the therapeutic potential and mechanism of action of lapatinib and other pan-ErbB inhibitors as a candidate broad-spectrum antiviral, anti-inflammatory and tissue protective strategy, with implications for future pandemic coronaviruses and beyond.

Results

High-throughput screening (HTS) for compounds that counteract SARS-CoV-2-induced lethality

We assembled a collection of 4,413 bioactive investigational and FDA approved compounds derived from four commercially available libraries and a self-assembled set of 13 kinase inhibitors (**Fig. 1a and Extended Data Fig. 1a**). This collection was screened in two independent experiments for inhibition of lethality induced by SARS-CoV-2 (isolate: Belgium-GHB-03021) in Vero E6 cells constitutively expressing an enhanced green fluorescent protein (eGFP) via a high-throughput assay[10] (**Fig. 1b**). The average percent fluorescent area for control wells included in each plate was 102.9±5% for uninfected cells (cell control), 0.1±0.2% for infected untreated cells (virus control), and 0.0±0.164% for infected cells treated with DMSO (**Fig. 1c**). The Z' and RZ' values of each of the 29 screen plates, calculated based on the virus control and cell control wells, were greater than 0.78 (**Extended Data Fig. 1b**). The signal-to-background (S/B) value, representing the ratio of the median value of the raw data between the virus control and the cell control, was greater than 120 (**Extended Data Fig. 1b**). The two replicate screens demonstrated good correlation (r= 0.76) (**Extended Data Fig. 1c**). Remdesivir

and its major metabolite, GS-441524, used as positive controls, demonstrated dose-dependent anti-SARS-CoV-2 activity in this assay (**Extended Data Fig. 1d)**. Overall, these data indicate that this antiviral assay is robust for HTS and is specific.

We set a percent area of greater than 15 in at least one of the two screens as the cutoff for positive hits (**Fig. 1c and Extended Data Fig. 2a**). 40 compounds from the commercial libraries and two from the kinase inhibitor set met this criterion. Nelfinavir and salinomycin, but not ivermectin, previously demonstrating anti-SARS-CoV-2 activity[9,11], emerged by our more stringent assay. Eighteen of the 42 hits were prioritized based on PubChem data documenting lower promiscuity and toxicity or activity against other viruses (**Fig. 1a**).

Dose-dependent effect of hits in an orthogonal antiviral assay

The 18 prioritized compounds were then studied for their effect on SARS-CoV-2 infection and cellular viability in Vero cells infected with a distinct viral isolate (2019-nCoV/USA-WA1/2020) via plaque and alamarBlue assays, respectively. Seven compounds showed potent dose-dependent antiviral activity with EC_{50} (half-maximal effective concentration) <0.7 μM, CC_{50} (half-maximal cellular cytotoxicity) >20 μM, and selectivity indices (SI, CC_{50} to EC_{50} ratio) >29 (**Fig. 1d, 1e and Extended Data Fig. 2b**). Six compounds showed moderate antiviral activity beyond toxicity with EC_{50} values of 1.2-4.3 μM, CC_{50}>20 μM, and SI>5.1. Four compounds effectively suppressed SARS-CoV-2 infection without apparent toxicity at the tested concentrations, albeit with higher EC_{50} values. Salbutamol showed no anti-SARS-CoV-2 activity (**Fig. 1d and Extended Data Fig. 2b**). In total, 17 hits demonstrated antiviral effect beyond toxicity, and 12 of these were effective at sub to low micromolar concentrations. These compounds target diverse cellular factors and functions (**Fig. 1f**). Two of the hits are known to target ErbBs: lapatinib (approved anticancer)[12] and tyrphostin AG 879 (experimental)[13]. Inhibitors of NUMB-associated kinases (NAK), heat shock protein 90 (HSP90) and ion transport across cell membranes were also among the hits. Five of the compounds have been previously approved for other indications and seven are natural products (**Fig. 1f**).

Broad-spectrum antiviral activity of hits

In parallel, we studied the effect of the 18 emerging hits on replication of two unrelated RNA viruses, the alphavirus Venezuelan equine encephalitis virus vaccine strain (VEEV (TC-83)), and the flavivirus, dengue (DENV2) in human astrocytes (U-87 MG) and hepatoma (Huh7) cells, respectively, both via luciferase assays. Lycorine, calcimycin, monensin, azaserine, gedunin, and the kinase inhibitors lapatinib and tyrphostin AG 879 dose-dependently inhibited replication of VEEV (TC-83) and DENV2 (**Extended Data Fig. 3**). Several compounds showed more potent anti-VEEV (TC-83) and DENV2 activity than anti-SARS-CoV-2 activity, and others showed variable activity against one or two of these viruses. Salbutamol demonstrated minimal to no activity against all three viruses (**Extended Data Fig. 2b and 3**).

Lapatinib has a broad-spectrum antiviral activity and a high genetic barrier to resistance

We focused on defining the therapeutic potential of lapatinib, an already approved pan-ErbB inhibitor that emerged in the screen (**Fig. 2a**). Lapatinib dose-dependently inhibited replication of SARS-CoV-2 (USA-WA1/2020 strain) in both Calu-3 (human lung epithelial) and Vero cells measured via plaque assays (EC_{50}=0.5-0.7 μM, CC_{50} >20 μM) (**Fig. 2b and 1e)**. Moreover, lapatinib demonstrated a dose-dependent rescue of Vero-eGFP cells from SARS-CoV-2-induced lethality (Belgium-GHB-03021 strain) (**Fig. 2c, d**).

Lapatinib dose-dependently inhibited infections of both vaccine (TC-83) and wild type (WT) (Trinidad donkey, TrD) VEEV measured by plaque assays in U-87 MG cells (EC_{50}=0.8 μM, CC_{50} >20 μM) (**Fig. 2e, f**). Similarly, it dose-dependently inhibited the replication of DENV2 (EC_{50}=1.8 μM) measured via plaque assays, and the filoviruses Ebola (EBOV) (EC_{50}=2.5 μM) and Marburg viruses (MARV) (EC_{50}=1.9 μM) measured via microneutralization assays in Huh7 cells, albeit lower CC_{50} values were measured in infected Huh7 cells (10.2-10.5 μM) relative to the other cell lines (**Fig. 2g-i**).

To determine whether viruses can escape treatment with lapatinib, we focused on VEEV (TC-83) since it replicates robustly in cultured cells, has a short life cycle, and its handling does not require BSL3 containment. VEEV was passaged in U-87 MG cells in the presence of lapatinib or the nonstructural protein 2 (nsP2) inhibitor ML336[14] and viral titers were measured in culture supernatants by plaque assays. By passage 3, VEEV overcame inhibition by ML336. In contrast, VEEV remained suppressed for 10 passages under lapatinib treatment without phenotypic resistance (**Fig. 2j**). Virus obtained from culture supernatants at passage 10 under lapatinib or DMSO treatment remained susceptible to lapatinib (**Fig. 2k**). Conversely, virus obtained at passage 10 under ML336, but not DMSO, treatment, lost its susceptibility to ML336, with the emergence of a resistance mutation in nsP2 (Y102C in TC-83) (**Fig. 2l**).

These results point to lapatinib as a potential broad-spectrum antiviral agent with a higher relative barrier to resistance than a direct-acting antiviral.

Lapatinib inhibits SARS-CoV-2 entry

To understand lapatinib's target(s) and mechanism of antiviral action, we first tested the hypothesis that by targeting receptor tyrosine kinases, it inhibits the entry of vesicular stomatitis virus encapsidated RNA pseudotyped with the SARS-CoV-2 spike glycoprotein (rVSV-SARS-CoV-2-S). Treatment of Calu-3 and Vero cells with lapatinib dose-dependently suppressed rVSV-SARS-CoV-2-S infection measured by luciferase assays without impacting cell viability (EC_{50}=2.6-3.2 μM, CC_{50} >20 μM) (**Fig. 3a, b and Extended Data Fig. 4a**). Moreover, lapatinib suppressed the level of intracellular viral RNA at 3 hours post-infection with a high rVSV-SARS-CoV-2-S inoculum measured via RT-qPCR (**Fig. 3a, c**). These results highlight a defect in the entry step, yet, it is possible that lapatinib inhibits additional stages of the SARS-CoV-2 life cycle.

ErbB4, but not other lapatinib's targets, is essential for SARS-CoV-2 entry and VEEV (TC-83) infection

The ErbB family is composed of four members (ErbB1-4), of which three are catalytically active: ErbB1, 2 , and 4[15]. Lapatinib's cancer targets are ErbB1 (EGFR) (IC_{50}=5.3 nM) and ErbB2 (HER2) (IC_{50}=35 nM)[12]. Yet, its kinome (ID:20107) reveals potent binding to 5 additional kinases (ErbB4, RAF1, RIPK2, STK10, and MAP2K5), with an overall excellent selectivity. To define which of these 7 molecular targets mediate(s) the observed antiviral effect of lapatinib, we studied the effects of siRNA-mediated depletion of these kinases on rVSV-SARS-CoV-2-S and VEEV (TC-83) infections. Depletion of ErbBs by siRNA pools was confirmed (**Extended Data Fig. 4b, c**). ErbB4 depletion suppressed rVSV-SARS-CoV-2-S infection in Vero cells by 73% (**Fig. 3d, e**) and VEEV (TC-83) infection in U-87 MG cells by 76% relative to non-targeting (NT) controls (**Extended Data Fig. 4d, e)**. RIPK2 depletion mildly reduced VEEV infection, but not rVSV-SARS-CoV-2-S infection (**Fig. 3e and Extended Data Fig. 4e**). Depletion of the remaining 5 targets, including ErbB1 and ErbB2, had no effect on infection of both viruses. None of these siRNA pools impacted cellular viability (**Fig. 3e and Extended Data Fig. 4e**).

Silencing ErbB4 expression by two siRNAs targeting distinct regions suppressed rVSV-SARS-CoV-2-S infection by 80-85% and VEEV (T-83) infection by 60-95% relative to siNT (**Fig. 3f, g and Extended Data Fig. 4f, g**). Moreover, these siErbB4s suppressed WT SARS-CoV-2 infection by 78-97% and SARS-CoV-2 entry by 50-80% relative to siNT (**Fig. 2d, f, h, i)**. ErbB4 depletion did not impact cell viability (**Fig. 3e, g, h and Extended Data Fig. 4e, g**) and largely correlated with the observed phenotype. These findings confirm a role for ErbB4 in viral entry; a step of the viral life cycle that is also inhibited by lapatinib.

Lapatinib was shown to bind the ATP binding site of ErbB4 in a comparable manner to ErbB1 and ErbB2 binding[16]. We measured an IC_{50} of 28 nM on ErbB4 in a cell-free assay (vs. IC_{50}=430 nM reported with a different peptide[17]) and confirmed anti-ErbB2 activity (**Extended Data Fig. 4h)**.

To further probe the requirement for ErbBs in SARS-CoV-2 infection, we evaluated the antiviral effect of chemically distinct compounds with anti-ErbB activity. Tyrphostin AG 879[13], an experimental compound that emerged in the HTS, dose-dependently inhibited SARS-CoV-2 and rVSV-SARS-CoV-2-S infections in Calu-3 cells (EC_{50}=0.5-1.1 μM, CC_{50}>20 μM (**Fig. 3j and Extended Data Fig. 4i**). Yet, its activity on ErbB2 and 4 could not be confirmed (**Extended Data Fig. 4h**), suggesting that another target may mediate its antiviral activity. While not included in the original screen, ibrutinib (**Fig. 3k)**, an approved anticancer Bruton's tyrosine kinase (BTK) inhibitor, and sapitinib (investigational) (**Fig. 3l)**, with potent pan-ErbB activity[12,18], suppressed both SARS-CoV-2 and rVSV-SARS-CoV-2-S infections, with EC_{50} values at sub to low micromolar range and CC_{50}>20 μM (**Fig. 3k-m and Extended Data Fig. 4h-j**).

Collectively, these results provide evidence that ErbB4, but not ErbB1 or 2, is required for SARS-CoV-2 entry and VEEV (TC-83) infection, thereby validating it as a druggable antiviral target. Its role as an entry co-factor, a step of the life cycle that is inhibited by lapatinib, supports a hypothesis that inhibition of ErbB4 mediates the antiviral effect of lapatinib.

ErbB4 is a molecular target mediating the antiviral effect of lapatinib

To determine whether lapatinib exerts its antiviral effect by inhibiting phosphorylation of ErbBs, lysates derived from SARS-CoV-2-infected Calu-3 cells treated with lapatinib or DMSO were subject to Western blot analysis. Lapatinib treatment dose-dependently suppressed the ratio of phosphorylated to total ErbB1, 2, and 4 levels at 24 hours post-infection with EC_{50} values lower than 0.1 μM that correlated with reduced expression of the SARS-CoV-2 nucleocapsid protein (**Fig. 4a, b)**. Similar findings were observed at 1.5 hour post-infection (**Extended Data Fig. 5**). These results provide evidence that drug exposure and the antiviral effect of lapatinib are correlated with functional inhibition of ErbBs' activity.

To confirm that inhibition of ErbB4 is a mechanism underlying the antiviral effect of lapatinib, we conducted gain-of-function assays. Ectopic expression of WT ErbB4, but not catalytically inactive ErbB4 mutant harboring a lysine to arginine substitution in position 751 (K751R) or control plasmid, either completely or partially reversed the antiviral effect of lapatinib on rVSV-SARS-CoV-2-S infection (**Fig. 4c-e and Extended Data Fig. 6a**). Similarly, WT, but not the ErbB4 mutant, reversed the effect of lapatinib on VEEV (TC-83) infection (**Extended Data Fig. 6b-e).** These results validate ErbB4 as a key mediator of the antiviral effect of lapatinib and indicate that its enzymatic activity is required for viral infection.

Lapatinib inhibits SARS-CoV-2-induced activation of ErbB-regulated inflammatory and tissue injury signals

In non-infectious ALI and ARDS, animal and human data indicate that ErbB1 and 2 are key regulators of inflammation and tissue injury via activation of the p38 MAPK, AKT/mTOR and Ras/RAF/MEK/ERK pathways[15,19-27]. To test the hypothesis that these pathways are activated in SARS-CoV-2 infection and suppressed by the pan-ErbB inhibitory effect of lapatinib, we measured their activation in Calu-3 cells upon SARS-CoV-2 infection and/or lapatinib treatment by Western blot analysis. At 1.5 and 24 hours post-infection, SARS-CoV-2 increased the ratio of phosphorylated to total protein level of AKT, ERK, and/or p38 MAPK by >1.5-2.5 fold (**Fig. 4b, f**), in agreement with reports in other cell lines[8,28]. Lapatinib treatment dramatically inhibited SARS-CoV-2-induced activation of AKT and ERK both at 1.5 and 24 hours post-infection and of p38 MAPK at 24 hours post-infection (**Fig. 4b, f**).

These results provide evidence that lapatinib inhibits SARS-CoV-2-induced activation of signaling pathways downstream of ErbBs, which are implicated in non-infectious ALI/ARDS.

Lapatinib inhibits SARS-CoV-2 infection, inflammation, and tissue injury *ex vivo* in human adult lung organoids (ALO)

Next, we studied the effect of lapatinib treatment on SARS-CoV-2 infection in a biologically relevant, validated human ALO monolayer model. Generated from adult stem cells isolated from lung tissue, these organoids contain both proximal airway cells, critical for sustained viral infection, and distal alveolar cells, required for mounting the overzealous host immune response

in fatal COVID-19[29] (**Fig. 5a**). Viral replication measured by plaque assays in culture supernatant and nucleocapsid transcript expression measured by RT-qPCR in ALO monolayer lysates both peaked at 48 hours following SARS-CoV-2 infection (**Extended Data Fig. 7a, b**), and were effectively suppressed by lapatinib, with EC_{50} values of 0.4 μM and <0.2 μM, respectively, and CC_{50} > 20 μM (**Fig. 5a-c**). Confocal immunofluorescence (IF) analysis revealed a near-complete disappearance of SARS-CoV-2 nucleocapsid staining in epithelial cell clusters forming alveolar-like structures and resembling AT2 cells in ALOs treated with 10 μM of lapatinib relative to DMSO controls (**Fig. 5d and Extended Data Fig. 7c**).

As in Calu-3 cells, lapatinib treatment dose-dependently inhibited phosphorylation of ErbB1, 2 and 4, indicating an association between its antiviral effect and ErbB modulation in these ALOs (**Fig. 5e**). Moreover, lapatinib treatment inhibited SARS-CoV-2-induced phosphorylation of AKT and ERK, albeit not p38 MAPK, in this more complex tissue model (**Fig. 5f**).

To test the hypothesis that ErbB-regulated signaling mediates the inflammatory response to SARS-CoV-2 infection, we measured cytokine levels in ALO culture supernatants upon SARS-CoV-2 infection and treatment with lapatinib or DMSO. SARS-CoV-2 infection increased the production of TNF-α, IL-1β and IL-6, in agreement with former reports[30]. Lapatinib treatment dose-dependently reduced the expression level of these pro-inflammatory cytokines, with levels at or lower than those measured in uninfected organoids achieved at drug concentration of 0.5 μM (**Fig. 5g**). Concurrently, lapatinib increased the expression level of MCP-1 (**Fig. 5g**), suggesting that it may augment innate immune responses[31].

Lastly, to define the role of ErbB signaling in SARS-CoV-2-induced lung injury, we analyzed the effect of lapatinib on the integrity of tight junction formation in ALOs via confocal IF analysis. Lapatinib was added to ALO monolayers 4 hours post-infection, to minimize its direct antiviral effect. Claudin 7 staining of uninfected ALOs revealed a continuous membranous pattern (**Fig. 5h, i and Extended Data Fig. 7d**). Thirty-six hours following SARS-CoV-2 infection and DMSO treatment, claudin 7 stained as speckles or short segments that often appeared in the cytoplasmic region. This finding was accompanied by cell separation and destruction of the alveolar-like architecture. In contrast, ALOs treated with 10 μM of lapatinib exhibited intact claudin 7 morphology and subcellular distribution and preserved architecture of the alveolar-like structure, comparable to uninfected controls (**Fig. 5h, i and Extended Data Fig. 7d).**

Together, these findings reveal regulation of SARS-CoV-2 infection, inflammation and epithelial barrier injury via ErbBs and provide a proof of concept for the utility of pan-ErbB inhibitors in suppressing these processes in a model that recapitulates COVID-19 pathology.

Discussion

Seventeen compounds targeting a diverse repertoire of functions that suppress SARS-CoV-2 infection and protect cells from its lethality, some with a broad-spectrum antiviral activity, emerged from our HTS. We integrated virology, biochemistry, genetic, immunological, and pharmacological approaches with a unique human lung organoid model to define the

therapeutic potential of lapatinib, an approved pan-ErbB inhibitor, as an antiviral agent and characterize its mechanism of action.

Our findings point to lapatinib and other pan-ErbB inhibitors as a class of broad-spectrum antiviral agents with a higher relative barrier to resistance than a classical direct-acting antiviral. Most antiviral strategies target viral enzymes, thereby typically providing a “one drug, one bug” approach that is prone to the emergence of viral resistance and is not easily scalable to meet the large unmet need[9,32]. While polymerase inhibitors, such as remdesivir and favipiravir, can suppress replication of unrelated viruses, the reported clinical benefit to date has been mild to moderate[2,9]. Lapatinib has recently emerged in an independent screen for anti-SARS-CoV-2 compounds in human lung fibroblasts[33] and in an *in silico* screen[34], but otherwise has not been studied for its antiviral activity or mechanism of antiviral action.

Using lapatinib as a pharmacological tool, we discovered ErbB4, the least studied ErbB, as a candidate antiviral target. Unlike other ErbBs, to the best of our knowledge, ErbB4 has not been previously implicated in the life cycle of a virus. Its precise role in viral entry, via fusion at the plasma membrane and/or endocytosis, remains to be elucidated. While writing this manuscript, ErbB4 was identified as a candidate interactor of the SARS-CoV-2 3C-like protease via an *in silico* approach[35], suggesting that it may also mediate later stages in the SARS-CoV-2 life cycle.

We provide multiple lines of evidence to support modulation of ErbB4 activity as an important mechanism of antiviral action of lapatinib. Lapatinib inhibits SARS-CoV-2 entry, analogous to the phenotype seen with RNAi-mediated ErbB4 suppression. Lapatinib’s antiviral activity correlates with reduced phospho-ErbB4 levels, and WT, but not a kinase dead ErbB4 mutant, reverses its antiviral effect against both SARS-CoV-2 entry and VEEV infection. This mechanism also plays a role *ex vivo* as evidenced by the correlation of antiviral activity with reduced ErbB4 phosphorylation in ALOs upon drug treatment. Inhibition of ErbB4 phosphorylation thus mechanistically explains, at least in part, the antiviral effect of lapatinib.

Independent of the role of ErbB4 in viral entry, we and others provide evidence that ErbBs are mediators of inflammation and lung injury. Human and animal data in multiple non-infectious ALI/ARDS models indicate that ErbBs are key regulators of inflammation, loss of epithelial barrier function, thrombosis, vasoconstriction, and the resulting fibrosis[15,19,25-27] - processes also involved in severe COVID-19 pathogenesis[9]. Indeed, transcriptomic and phosphoproteomic studies revealed that activation of ErbBs and/or their downstream pathways are among the strongest detected upon infection of human cells with SARS-CoV[36], SARS-CoV-2[8,28] and MERS[37], and in mice infected with SARS-CoV[38], proposing roles for these pathways in pan-coronaviral infections and/or pathogenesis. However, these signaling pathways have not been directly linked to SARS-CoV-2-induced inflammation and lung injury. In human lung epithelium and organoids, we demonstrate SARS-CoV-2-induced activation of p38 MAPK, AKT, and ERK and inhibition of phosphorylation of both ErbBs and these downstream effectors by lapatinib. Moreover, in human ALOs, we show that SARS-CoV-2 infection increases production of pro-inflammatory cytokines and disrupts the lung epithelial barrier integrity and that lapatinib treatment effectively suppresses both processes. These results establish a role for ErbB

pathways in SARS-CoV-2-induced inflammation and acute lung injury and propose pan-ErbB inhibition as an effective means to disrupt these processes.

Based on our and the cumulative published data, we propose a model wherein ErbB4 is required for SARS-CoV-2 entry, while pan-ErbB activation of downstream signaling pathways by SARS-CoV-2 mediates inflammation and lung injury. By suppressing both processes, pan-ErbB inhibitors, not only inhibit viral infection, but independently also reduce inflammation and tissue injury (**Fig. 6**).

We predict that the anti-inflammatory and tissue protective effects of lapatinib are beyond its ErbB4-mediated antiviral effect. First, these effects correlate with suppression of relevant signaling pathways. Second, the tissue protective effect was observed when lapatinib was added 4 hours post-infection, i.e. following the first round of viral entry. Third, lapatinib was shown to reverse increased epithelium permeability in a non-infectious (IL-1β –induced), *in vitro* lung injury model[20]. Fourth, while lapatinib has not been studied in non-infectious mouse models of ALI, AG1478, an investigational ErbB1 inhibitor diminished lung alveolar permeability, vascular leak, and neutrophil accumulation in the BAL in a mouse model of mechanical ventilation-induced ALI [39].

Beyond ALI, ErbB1 and 2 are implicated in lung fibrosis[22-24]. Most relevant, ErbB1 was shown to mediate SARS-CoV-induced fibrosis independently of viral titers in a STAT1-/- mouse model [38]. Notably, various ErbB1 and 2 inhibitors reduced lung fibrosis, morbidity and/or mortality in bleomycin- and TGF-α induced lung fibrosis mouse models[21,40,41]. We thus predict that lapatinib may also protect from lung fibrosis.

While it remains to be experimentally proven, since ErbB1 has been shown to be required for SARS-CoV infection[42], and the pathways downstream of ErbBs are similarly upregulated in SARS-CoV and MERS, we predict that this model applies to other pandemic coronaviral infections.

ErbBs mediate the deleterious effects of multiple ligands implicated in ALI and lung fibrosis, such as NRG-1, TGF-α, HB-EGF, and AREG, some of which have shown to play a role in coronaviral infections[19,23,24,43]. Moreover, unopposed Angiotensin (Ang) II effect activates ErbB pathways[44] and was linked to increased pulmonary vascular permeability in animal models of non-viral lung injury[45], whereas Ang (1–7) acts as a pan-ErbB inhibitor[46]. It is thus intriguing to speculate that the imbalance in the renin angiotensin system (RAS), thought to play a major role in the pathogenesis of severe coronaviral infections[9,47], contributes to the observed activation of ErbB pathways. By inhibiting ErbB activation by multiple ligands and Ang II, lapatinib should, at least in theory, achieve a greater anti-inflammatory and tissue protective effect from approaches that target individual components of these pathways (e.g. Ang (1-7), antibodies targeting IL-1β, TGF-β and IL-6, and p38 MAPK inhibitors) (**Fig. 6**).

Collectively, these findings provide insight into the mechanisms underlying the antiviral, anti-inflammatory, and tissue protective effects of lapatinib. The approaches being studied for

COVID-19 to date typically target one of these processes, but not all three. Demonstrating these effects in the biologically relevant human ALO model illuminates the translatability of this approach. While lapatinib has not been studied for COVID-19 treatment to date, ibrutinib has shown protection from progression to severe COVID-19, albeit in a small number of patients[48]. This protection was thought to be mediated solely by ibrutinib's anti-inflammatory effect via its cancer target, BTK. Nevertheless, beyond its anti-BTK activity, ibrutinib is a potent pan-ErbB inhibitor[12] (**Fig. 3m**). Indeed, we show that like lapatinib, ibrutinib inhibits SARS-CoV-2 infection. Our data provide evidence that pan-ErbB inhibition by ibrutinib mediates, at least in part, the observed protective effect. Our findings thus provide insight into the mechanism of action of another repurposed candidate for COVID-19 and propose additional investigational pan-ErbB inhibitor candidates (e.g. sapitinib).

Repurposing existing drugs requires less capital and time and diminishes the clinical risks, as such drugs have already been tested (toxicity, pharmacokinetics (PK), dosing, etc.) for their primary indication[9]. Lapatinib is an oral drug that is approved globally in combination drug treatments for metastatic, ErbB2-positive breast cancer. Based on the available PK data, the plasma and hence lung level achieved with the approved dose of lapatinib (1500 mg once daily) should be therapeutic as it is 8-10 fold higher than the EC_{50}s we measured for its anti-SARS-CoV-2 effect in ALOs. Even higher lapatinib lung levels may be achieved, as suggested by the predicted lung to plasma area under the curve ratio of 8.2-10[49]. Although toxicity is a concern when targeting host functions, lapatinib has a favorable safety profile, particularly when used as a monotherapy and for short durations, as those required to treat acute infections. A summary of safety considerations and drug-drug interactions is provided in Supplementary Discussion.

Other compounds targeting diverse cellular factors and functions have emerged in the HTS. A summary of other compounds, their predicted targets and reported antiviral activity is provided in Supplementary Discussion. One example is sunitinib, a multi-kinase inhibitor that we have shown to protect mice from DENV and EBOV challenges when given in combination with erlotinib by inhibiting NAK-mediated intracellular viral trafficking[50,51]. Sunitinib was recently shown to suppress pan-corona pseudotyped viral infections[52]. Compounds targeting ion transport across cell membranes, HSP90 and others are additional examples. These findings reveal candidate targets for anti-SARS-CoV-2 approaches.

In summary, our study validates ErbBs as druggable targets for antiviral, anti-inflammatory and tissue protective approaches and proposes approved drugs with anti-pan-ErbB activity as an attractive class of repurposing candidates for COVID-19 that may provide readiness for future outbreaks of coronaviruses and other emerging viruses. The safety and efficacy of pan-ErbB inhibition as an anti-coronaviral strategy therefore warrants clinical evaluation particularly in hospitalized patients with comorbidities and/or low oxygen requirements.

Methods:

Compound libraries and reagents. The 4 commercial libraries (Microsource Spectrum library of 2000 compounds, the two Biomol collections of 480 known diverse bioactive compounds with defined biological activity and 640 FDA-approved drugs, and the LOPAC collection of 1280 pharma-developed tools and approved drugs) were available at the Stanford High-Throughput Bioscience Center. Small molecule inhibitors were purchased from MedchemExpress or from Cayman Chemical except for Ac-Leu-Leu-Nle-CHO (BML-P120, Enzo Life Sciences), tesevatinib (A110575, Adooq Bioscience LLC), and erlotinib (E-4007, LC Laboratories). Dinaciclib and ribociclib were a gift from Dr. Mardo Koivomaegi (Stanford University).

High-throughput screening (HTS) of compound libraries. Compounds from the libraries listed above were plated in a total of 29 assay-ready 384-well plates (Greiner #7810192). Dispensing of 6 µl of the compound solutions was achieved using an automated Agilent Bravo pipetting system, allowing for a final test concentration of 10 µM (or 10-20 in the case of the self-assembled kinase inhibitor collection). The HTS was based on an assay previously developed to discover antiviral agents for SARS-CoV infection[53]. Briefly, 30 µL Vero-E6-eGFP cells were added at 8000 cells/well to columns 1-24 24 hours before infection. 30 µL assay medium was added to columns 23 and 24, which were used as cell controls. Following a 20-hour incubation, cells in columns 1-22 were infected with 30 µL SARS-CoV-2 (Belgium-GHB-03021) at an MOI of 0.001, using an automated, no-contact liquid handler (EVO 100, Tecan) on the Caps-It robotics system. Plates were then incubated for 4 days and imaged via a high content imager (Arrayscan XTI, Thermofisher) using wide-field fluorescence microscopy. eGFP signal was used as a marker for survival from viral-induced lethality. The cells were excited at 485-20 nm and emission was captured via a CCD camera and a BGRFRN_BGRFRN dichroic mirror and filter set. A 5X objective was used so that 1 single image contains approximately 75% of a well surface. The exposure time was set at 0.023 seconds, as determined by the fluorescent intensity signal in the control wells. Imaging acquisition speed was optimized using a 2x2 binning on 1104x1104 pixel resolution and reducing the number of autofocus focal planes. The Cellomics (Thermofisher) software was used for image analysis. A custom-made image analysis protocol was created using the SpotDetector bioapplication. First, a background reduction was performed on the raw images to remove non-specific fluorescent signal. Second, a fixed fluorescent intensity threshold was determined to identify eGFP signal. Lastly, the total surface area occupied by eGFP signal was calculated from the processed images. The selected output feature was ‘SpotTotalAreaCh2’ and was used for further data analysis.

Hit selection. The entire compound collection was screened in two independent experiments. Data were normalized to the median of each plate. The *Z*-score was calculated on the basis of the log2(fold change) (log2FC) with the average and standard deviation of each plate. 40 compounds from the screen were selected according to the cutoff of fluorescence % area greater than 15 in at least one of the two screens, which is 15 times greater than the values obtained with untreated or DMSO treated cells.

Plasmids. Plasmids used in the production of SARS-CoV-2 pseudovirus were a gift from Jing Lin (Vitalant, San Francisco). Plasmid encoding VEEV TC-83 with a nanoluciferase reporter (VEEV TC-83-Cap-nLuc-Tav) was a gift from Dr. William B. Klimstra (Department of Immunology, University of Pittsburgh)[54]. DENV2 (New Guinea C strain) TSV01 Renilla reporter plasmid (pACYC NGC FL) was a gift from Pei-Yong Shi (University of Texas Medical Branch, Galveston, Texas, USA)[55]. pDONR223-ErbB4 was a gift from William Hahn & David Root (Addgene plasmid # 23875 ; http://n2t.net/addgene:23875 ; RRID:Addgene_23875) [56]. The ORF was recombined into a gateway compatible pGluc destination vector using Gateway technology (Invitrogen) and the construct was verified using Sanger sequencing. Mutations were introduced by site-directed mutagenesis using the QuikChange Lightning Site-Directed Mutagenesis Kit (Agilent).

Viral stocks preparation and/or passaging. Belgium-GHB-03021 SARS-CoV-2 strain was recovered from a nasopharyngeal swab taken from an asymptomatic patient returning from Wuhan, China early February 2020[57] and passaged 6 times on Huh7 and Vero E6 cells. Viral titer was quantified by means of endpoint titrations on confluent Vero E6 cell cultures, calculated using the Spearman-Kärber method, and expressed as 50% tissue culture infectious dose ($TCID_{50}$)/ml. All Belgium-GHB-03021 SARS-CoV-2-related work was conducted in the high-containment BSL3+ facilities of the KU Leuven Rega Institute (3CAPS) under licenses AMV 30112018 SBB 219 2018 0892 and AMV 23102017 SBB 219 2017 0589 according to institutional guidelines.

The USA-WA1/2020 SARS-CoV-2 strain was received from BEI Resources and passaged 3-6 times in Vero E6 cells in DMEM supplemented with 2% FBS. Viral stock titers were determined by standard plaque assay on Vero E6 cells, as described[58].

VEEV-TC-83-nLuc RNA was transcribed *in vitro* from cDNA plasmid templates linearized with MluI via MEGAscript SP6 kit (Invitrogen #AM1330) and electroporated into BHK-21 cells. Similarly, DENV RNA was transcribed *in vitro* from pACYC-DENV2-NGC plasmid by mMessage/mMachine (Ambion) kits and electroporated into BHK-21 cells. For both viruses, the supernatants were harvested after 24 hours post electroporation, clarified and stored at -80 °C. WT Trinidad Donkey (TrD) VEEV strain, EBOV (Kikwit isolate) and MARV (Ci67 strain) were obtained from BEI Resources. EBOV and MARV were grown in Vero E6 cells. Viral stock titers were determined via standard plaque assays on BHK-21 for DENV and VEEV or on Vero E6 cells for EBOV and MARV.

USA-WA1/2020 SARS-CoV-2- and WT VEEV-related work was conducted in the high-containment BSL3 facilities of Stanford University and George Mason University according to CDC and institutional guidelines. EBOV and MARV work was conducted at the high-containment BSL4 facilities at the United States Army Medical Research Institute of Infectious Diseases.

Viral sequencing. All SARS-CoV-2 stocks were deep sequenced on a MiSeq platform (Illumina).

For the HTS of compound library, Belgium/GHB-03021/2020 SARS-CoV-2 from passage 6 (P6) was used. The viral stock was deep sequenced following an established metagenomics pipeline [59]. 100% of the viral reads of P6 GHB-03021/2020 SARS-CoV-2 harbored a deletion of the multi-basic cleavage (MBC) domain, as reported[59].

The rest of the experiments were done using the USA-WA1/2020 strain. SARS-CoV-2 whole-genome amplicon-based sequencing was conducted by adapting an existing whole genome sequencing pipeline for poliovirus genotyping[60]. Dose response curves with lapatinib in Calu-3 and Vero cells (**Fig. 1e, 2b and Extended data fig. 2b**) were performed with a P3 USA-WA1/2020 SARS-CoV-2 virus harboring no deletion or point mutations in the MBC domain. The remaining experiments were performed using a P6 USA-WA1/2020 SARS-CoV-2 containing mixed populations, of which the majority (51%-80%) had WT sequence with no MBC deletion.

Cells. The African green monkey kidney cell line (Vero E6) constitutively expressing the enhanced green fluorescent protein (eGFP) used for antiviral screening purposes was kindly provided by Dr. Marnix Van Loock (Janssen Pharmaceutica, Beerse, Belgium)[53]. Cells were maintained in Dulbecco's modified Eagle's medium (DMEM; Gibco) supplemented with 10% v/v fetal calf serum (FCS; Biowest), 0.075% sodium bicarbonate (7.5% solution, Gibco) and 1x Pen-strep (Gibco). The assay medium was DMEM, supplemented with 2% FCS. Vero E6 (ATCC) were maintained in DMEM (10-013-CV, Corning) supplemented with 10% fetal bovine serum (FBS, Omega Scientific, Inc), 1% L-glutamine 200mM (Gibco), 1% penicillin-streptomycin (Gibco), 1% nonessential amino acids (Gibco), 1% HEPES (Gibco), 1% Sodium pyruvate (Thermofisher scientific). Vero (ATCC), HEK-293T (ATCC), U-87 MG (ATCC), and BHK-21 (ATCC) cells were grown in DMEM (10-013-CV, Corning) supplemented with 10% FBS (Omega Scinetific, Inc), and 1% penicillin-streptomycin. Huh7 cells (Apath LLC) and Calu-3 cells (ATCC) were grown in DMEM (10-013-CV, Corning) supplemented with 10% FBS (Omega Scinetific, Inc), 1% l-glutamine, 1% nonessential amino acids (Corning) and 1% penicillin-streptomycin (Gibco). All the cells were maintained in a humidified incubator with 5% CO_2 at 37°C. All cells were tested negative for mycoplasma by the MycoAlert mycoplasma detection kit (Lonza, Morristown, NJ).

Human adult lung organoids and organoid-derived monolayers for SARS-CoV-2 infection. The human adult lung organoid (ALO) model containing proximal and distal features of airway epithelia was generated from adult stem cells isolated from deep lung biopsy specimens[29]. The organoids from these lung tissues were isolated and propagated using an approved human research protocol (IRB# 190105: PI Ghosh and Das) that covers human subject research at the UC San Diego HUMANOID Center of Research Excellence (CoRE). The lung organoid model is complete with all 6 cell types of proximal and distal airways as validated previously[29]. Lung-organoid-derived single cells were prepared[29] and plated in Pneumacult Ex-Plus Medium (StemCell, Canada). After 2 days, monolayers were infected with SARS-CoV-2 (USA-WA1/2020 strain) at an MOI of 1.

rVSV-SARS-CoV-2-S production. HEK-293T cells were transfected with 30 µg of Spike (S) expression plasmid. Twenty-four hours post-transfection, the medium was replaced and cells

were treated with DMEM containing 3.75 mM valproic acid (VPA) for 4 hours. The medium was then removed, and cells were infected with VSV-G pseudotyped ΔG-luciferase VSV virus (MOI=3). Six hours post-infection, cells were washed with PBS and fresh medium containing anti-VSV-G hybridoma was added to neutralize the residual VSV-G pseudovirus. Culture supernatant was harvested after 24-hour incubation, clarified by centrifugation, filtered (0.22 μm) and stored at -80°C. The $TCID_{50}$ of rVSV-SARS-CoV-2-S pseudovirus was determined via luciferase assay 24 hours after infection of Vero cells. Positive wells were defined as having luminescence unit (RLU) values at least 10-fold higher than the cell background.

Western blotting and antibodies. Cells were lysed in M-Per protein extraction reagent (Thermo Fisher Scientific) or RIPA buffer containing 1% NP40 supplemented with Halt protease and phosphatase inhibitor cocktail (Thermo Fisher Scientific). Clarified lysates were run on 4%–12% Bis-Tris gels (Invitrogen), transferred onto PVDF membranes (Bio-Rad). Blots were blocked with 5% BSA/TBST and blotted with anti-ErbB4 (Santa Cruz), ErbB2 (Cell Signaling), ErbB1, AKT, ERK, p38 (Cell Signaling), P-ErbB4 (Tyr1284), P-ErbB2(Tyr1248), P-AKT(Ser473), P-ERK(Thr202/Tyr204), P-p38 (Thr180/Tyr182) (Cell Signaling), and β-actin (Sigma-Aldrich, catalog A3854) antibodies. Signal was detected with HRP-conjugated secondary antibodies. Band intensity was quantified with ImageJ software (NIH).

RNA interference. siRNAs (10 pmol/96-well) were transfected into cells using lipofectamine RNAiMAX transfection reagent (Invitrogen) 48 hours prior to infection with VEEV-TC-83-nLuc at MOI of 0.01, rVSV-SARS-CoV-2-S or SARS-CoV-2 (USA-WA1/2020). ON-TARGETPlus siRNA SMARTpools against 7 genes and non-targeting siRNA (siNT) were purchased from Dharmacon/Horizon Discovery with gene IDs as follows: EGFR (1956), ErbB2 (2064), ErbB4 (2066), RIPK2 (8767), RAF1 (5894), STK10 (6793), MAP2K5 (5607). Single ErbB4 siRNAs were ordered from Millipore Sigma (ErbB#1 GCAAGAAUUGACUCGAAU, ErbB#2 CCUCAAAGAUACCUAGUUA).

Infection assays. Calu-3 cells, Vero cells or ALOs were infected with SARS-CoV-2 in triplicates (MOI=0.05 or 1) in DMEM containing 2% FCS at 37°C under biosafety level 3 (BSL3) conditions. After 1 to 3-hour incubation, the inoculum was removed, cells were washed and supplemented with new medium. At various time points post-infection, culture supernatants were harvested for measurement of viral titer by standard plaque assays and cells were lysed in Trizol for RT-qPCR analysis. Huh7 cells were infected with DENV2 in replicates (n = 3-10) at an MOI of 0.05. Overall infection was measured at 48 hours using a *Renilla* luciferase substrate or a standard plaque assay. Huh7 cells were infected with EBOV (MOI=1) or MARV (MOI=2) under BSL4 conditions. 48 hours post-infection cells were formalin-fixed for 24 hours prior to removal from BSL4. Infected cells were detected using an EBOV or MARV glycoprotein-specific monoclonal antibody (KZ52 and 7E6, respectively) and quantitated by automated fluorescence microscopy using an Operetta High Content Imaging System and the Harmony software package (PerkinElmer). U-87 MG cells were infected with VEEV-TC-83-nLuc in 8 replicates at MOI of 0.01. Overall infection was measured at 24 hours post-infection via a nanoluciferase assay using a luciferin solution obtained from the hydrolysis of its O-acetylated precursor, hikarazine-103 (prepared by Dr. Yves Janin, Institut Pasteur, France) as a substrate[61] or

standard plaque assay. U-87 MG cells were infected with WT VEEV TrD in triplicates and at 24 hours post-infection the viral titer was measured via standard plaque assays.

Pharmacological inhibition. Inhibitors or DMSO were added to the cells 1 hour prior to viral inoculation and were left for the duration of the experiment. Viral infection was measured via luciferase (DENV2, VEEV (TC-83)) or plaque (SARS-CoV-2, VEEV-TrD, VEEV (TC-83), DENV2) assays. Immunofluorescence assay with anti-GP probe was used for EBOV and MARV.

Entry assays. Vero cells were infected with virulent SARS-CoV-2 (MOI=1) or a high inoculum of rVSV-SARS-CoV-2-S. Following 1-hour incubation, the viral inoculum was removed, cells were washed three times with PBS and replaced with fresh medium. At 3 hours post-infection, cells were lysed in TRIzol (Invitrogen) or RLT lysis buffer (RNeasy Mini Kit, Qiagen) and viral RNA levels were measured by RT-qPCR.

RT-qPCR. RNA was extracted from cell lysates using Direct-zol RNA Miniprep Plus Kit (Zymo Research) or RNeasy Mini Kit (Qiagen) and reverse transcribed using High-Capacity cDNA RT kit (Applied Biosystems) according to the manufacturer's instructions. Primers and PowerUp SYBR Green Master Mix (Applied Biosystems) were added to the samples, and PCR reactions were performed with QuantStudio3 (Applied Biosystems). Samples were analyzed in triplicates and target genes were normalized to the housekeeping gene. The following primers were used: GAPDH (F-GGAGCGAGATCCCTCCAAAAT;R-GGCTGTTGTCATACTTCTCATGG), ErbB1 (F-ACCACCCTGGTCTGGAAGTACG; R-TCGTTGGACAGCCTTCAAGACC); ErbB2 (F-GGAAGTACACGATGCGGAGACT; R-ACCTTCCTCAGCTCCGTCTCTT); ErbB4 (F-GGAGTATGTCCACGAGCACAAG; R-CGAGTCGTCTTTCTTCCAGGTAC) N-SARS-CoV2 (F-TAATCAGACAAGGAACTGATTA, R-CGAAGGTGTGACTTCCATG).

Viability assays. Viability was assessed using alamarBlue reagent (Invitrogen) according to the manufacturer's protocol. Fluorescence was detected at 560 nm on an InfiniteM1000 plate reader (Tecan).

Gain-of-function assays. Plasmids encoding WT ErbB4, ErbB4 mutant (K751R) or empty control were transfected individually into Vero or U-87 MG cells using Lipofectamine 3000 reagent (Invitrogen) 24 hours prior to drug treatment and infection with rVSV-SARS-CoV-2-S or VEEV-TC-83-nLuc, respectively. Viral infection and cell viability were measured 24 hours later via luciferase and alamarBlue assays, respectively.

Resistance studies. VEEV (TC-83) was used to inoculate U-87 MG cells at MOI of 0.1 and passaged every 24 hours by transferring an equal volume of viral supernatant to naive cells under increasing drug selection (2.5-5 μM, passages 1–3; 5-10 μM, passages 4-7; 10-15 μM, passages 8-10). Upon completion of 10 passages, viral titers were measured in culture supernatants by plaque assays. ML336 resistant mutation emerging in nsP2 at passage 10 was confirmed by purification and reverse transcription of viral RNA from cell supernatants using RNeasy Mini Kit (Qiagen) and SuperScript IV First-Strand Synthesis kit (Invitrogen) respectively.

The nsP2 region was amplified with Platinum Green Hot Start PCR Master Mix (2x) (Invitrogen) using the following primers: (forward: AGGAAAATGTTAGAGGAGCACAAG reverse: GTCAATATACAGGGTCTCTACGGGGTGT (and sequenced (Sequetech Corp.).

In vitro kinase assays. ErbB2 and ErbB4 *in vitro* kinase assays were performed on the LabChip platform (Nanosyn) or radiometric HotSpot™ kinase assay platform (Reaction Biology).

Signaling pathway analysis. Following a 2-hour starvation under serum-low or -free conditions, Calu-3 cells or ALOs were treated with lapatinib or DMSO and within an hour infected with SARS-CoV-2 (MOI=1). Cell lysates were obtained at 1.5 and/or 24 hours post-infection followed by Western blot analysis with antibodies targeting the phosphorylated and total forms of ErbB1, 2 and 4, p38/MAPK, ERK, and AKT. Phosphorylated to total protein ratios were quantified with ImageJ software (NIH).

Cytokine measurements in culture supernatants. A LEGENDplex Human Inflammation Panel 1 (Biolegend) kit was used following the manufacturer's instructions to measure the concentration of cytokines in culture supernatants derived from ALOs. Cytokine concentrations were measured via Quanteon (Agilent) and data analyzed using LEGENDplex V8.0 software.

Immunofluorescence and confocal microscopy. ALO cells were plated at a concentration of $2.5x10^6$ cell/well in a μ-Slide 8 well (ibidi) system. Lapatinib or DMSO were administered either an hour pre-infection or 4 hours post-infection with SARS-CoV-2 (MOI=1). At 24-, 36- and 48-hours post-infection, cells were washed with PBS and fixed with 4% PFA for 30 minutes at RT. Cells were blocked for 1h at RT with 3% BSA and 0.1 % Triton X in PBS. Cells were incubated with mouse mAb SARS-CoV-2 nucleocapsid antibody (SinoBiological, 1:100) and rabbit Claudin 7 polyclonal antibody (ThermoFisher, 1:200) overnight at 4°C, followed by 1 hour incubation at room temperature with goat anti-mouse AF488 (ThermoFisher, 1:400), goat anti-rabbit AF647 (ThermoFisher, 1:400), and counterstaining with DAPI (4', 6-diamidino-2-phenylindole, ThermoFisher, 1:10000) and phalloidin (ThermoFisher, 1:400). Images were taken on an SP8 microscope (Leica). Adjustment for brightness, contrast and color balance were done using Fiji software.

Quantification and Statistical Analysis. All data were analyzed with GraphPad Prism software. Fifty percent effective concentrations (EC_{50}) and 50% cytotoxic concentration (CC_{50}) were measured by fitting of data to a 3-parameter logistic curve. *P* values were calculated by one-way ANOVA with either Dunnett's or Tukey's multiple comparisons tests as specified in each Fig. legend.

References:

1 Wu, Z. & McGoogan, J. M. Characteristics of and Important Lessons From the Coronavirus Disease 2019 (COVID-19) Outbreak in China: Summary of a Report of 72 314 Cases From the Chinese Center for Disease Control and Prevention. *JAMA* **323**, 1239-1242, doi:10.1001/jama.2020.2648 (2020).

2 Beigel, J. H. *et al.* Remdesivir for the Treatment of Covid-19 - Final Report. *The New England journal of medicine*, NEJMoa2007764, doi:10.1056/NEJMoa2007764 (2020).

3 Horby, P. *et al.* Dexamethasone in Hospitalized Patients with Covid-19 - Preliminary Report. *The New England journal of medicine*, doi:10.1056/NEJMoa2021436 (2020).

4 Spagnolo, P. *et al.* Pulmonary fibrosis secondary to COVID-19: a call to arms? *The Lancet. Respiratory medicine* **8**, 750-752, doi:10.1016/S2213-2600(20)30222-8 (2020).

5 Jin, Z. *et al.* Structure of Mpro from COVID-19 virus and discovery of its inhibitors. *Nature*, doi:10.1038/s41586-020-2223-y (2020).

6 Riva, L. *et al.* Discovery of SARS-CoV-2 antiviral drugs through large-scale compound repurposing. *Nature* **586**, 113-119, doi:10.1038/s41586-020-2577-1 (2020).

7 Gordon, D. E. *et al.* A SARS-CoV-2 protein interaction map reveals targets for drug repurposing. *Nature* **583**, 459-468, doi:10.1038/s41586-020-2286-9 (2020).

8 Bouhaddou, M. *et al.* The Global Phosphorylation Landscape of SARS-CoV-2 Infection. *Cell* **182**, 685-712.e619, doi:10.1016/j.cell.2020.06.034 (2020).

9 Saul, S. & Einav, S. Old Drugs for a New Virus: Repurposed Approaches for Combating COVID-19. *ACS infectious diseases*, doi:10.1021/acsinfecdis.0c00343 (2020).

10 Ivens, T. *et al.* Development of a homogeneous screening assay for automated detection of antiviral agents active against severe acute respiratory syndrome-associated coronavirus. *J Virol Methods* **129**, 56-63, doi:10.1016/j.jviromet.2005.05.010 (2005).

11 Ianevski, A. *et al.* Potential Antiviral Options against SARS-CoV-2 Infection. *Viruses* **12**, doi:10.3390/v12060642 (2020).

12 Chen, J., Kinoshita, T., Sukbuntherng, J., Chang, B. Y. & Elias, L. Ibrutinib Inhibits ERBB Receptor Tyrosine Kinases and HER2-Amplified Breast Cancer Cell Growth. *Mol Cancer Ther* **15**, 2835-2844, doi:10.1158/1535-7163.Mct-15-0923 (2016).

13 Levitzki, A. & Gazit, A. Tyrosine kinase inhibition: an approach to drug development. *Science* **267**, 1782-1788, doi:10.1126/science.7892601 (1995).

14 Chung, D. *et al.* in *Probe Reports from the NIH Molecular Libraries Program* (National Center for Biotechnology Information (US), 2010).

15 Finigan, J. H., Downey, G. P. & Kern, J. A. Human epidermal growth factor receptor signaling in acute lung injury. *American journal of respiratory cell and molecular biology* **47**, 395-404, doi:10.1165/rcmb.2012-0100tr (2012).

16 Qiu, C. *et al.* Mechanism of activation and inhibition of the HER4/ErbB4 kinase. *Structure (London, England : 1993)* **16**, 460-467, doi:10.1016/j.str.2007.12.016 (2008).

17 Rusnak, D. W. *et al.* The effects of the novel, reversible epidermal growth factor receptor/ErbB-2 tyrosine kinase inhibitor, GW2016, on the growth of human normal and tumor-derived cell lines in vitro and in vivo. *Mol Cancer Ther* **1**, 85-94 (2001).

18 Hickinson, D. M. *et al.* AZD8931, an Equipotent, Reversible Inhibitor of Signaling by Epidermal Growth Factor Receptor, ERBB2 (HER2), and ERBB3: A Unique Agent for Simultaneous ERBB Receptor Blockade in Cancer. *Clinical Cancer Research* **16**, 1159-1169, doi:10.1158/1078-0432.Ccr-09-2353 (2010).

19 Finigan, J. H. *et al.* Neuregulin-1-human epidermal receptor-2 signaling is a central regulator of pulmonary epithelial permeability and acute lung injury. *The Journal of biological chemistry* **286**, 10660-10670, doi:10.1074/jbc.M110.208041 (2011).

20 Ma, X., Yu, X. & Zhou, Q. The IL1β-HER2-CLDN18/CLDN4 axis mediates lung barrier damage in ARDS. *Aging (Albany NY)* **12**, 3249-3265, doi:10.18632/aging.102804 (2020).

21 Faress, J. A. *et al.* Bleomycin-induced pulmonary fibrosis is attenuated by a monoclonal antibody targeting HER2. *Journal of applied physiology (Bethesda, Md. : 1985)* **103**, 2077-2083, doi:10.1152/japplphysiol.00239.2007 (2007).

22 Finigan, J. H. *et al.* HER2 activation results in β-catenin-dependent changes in pulmonary epithelial permeability. *American journal of physiology. Lung cellular and molecular physiology* **308**, L199-207, doi:10.1152/ajplung.00237.2014 (2015).

23 Hardie, W. D. *et al.* Reversal of lung lesions in transgenic transforming growth factor alpha mice by expression of mutant epidermal growth factor receptor. *American journal of respiratory cell and molecular biology* **15**, 499-508, doi:10.1165/ajrcmb.15.4.8879184 (1996).

24 Zhou, Y. *et al.* Amphiregulin, an epidermal growth factor receptor ligand, plays an essential role in the pathogenesis of transforming growth factor-β-induced pulmonary fibrosis. *The Journal of biological chemistry* **287**, 41991-42000, doi:10.1074/jbc.M112.356824 (2012).

25 Li, R. *et al.* HMGB1/PI3K/Akt/mTOR Signaling Participates in the Pathological Process of Acute Lung Injury by Regulating the Maturation and Function of Dendritic Cells. *Frontiers in Immunology* **11**, doi:10.3389/fimmu.2020.01104 (2020).

26 Zhang, X. L., Xing, R. G., Chen, L., Liu, C. R. & Miao, Z. G. PI3K/Akt signaling is involved in the pathogenesis of bleomycin-induced pulmonary fibrosis via regulation of epithelial-mesenchymal transition. *Molecular medicine reports* **14**, 5699-5706, doi:10.3892/mmr.2016.5960 (2016).

27 Zarubin, T. & Han, J. Activation and signaling of the p38 MAP kinase pathway. *Cell research* **15**, 11-18, doi:10.1038/sj.cr.7290257 (2005).

28 Appelberg, S. *et al.* Dysregulation in Akt/mTOR/HIF-1 signaling identified by proteo-transcriptomics of SARS-CoV-2 infected cells. *Emerging Microbes & Infections* **9**, 1748-1760, doi:10.1080/22221751.2020.1799723 (2020).

29 Tindle, C. *et al.* Adult Stem Cell-derived Complete Lung Organoid Models Emulate Lung Disease in COVID-19. *bioRxiv*, doi:10.1101/2020.10.17.344002 (2020).

30 Del Valle, D. M. *et al.* An inflammatory cytokine signature predicts COVID-19 severity and survival. *Nature medicine* **26**, 1636-1643, doi:10.1038/s41591-020-1051-9 (2020).

31 Sokol, C. L. & Luster, A. D. The chemokine system in innate immunity. *Cold Spring Harbor perspectives in biology* **7**, doi:10.1101/cshperspect.a016303 (2015).

32 Bekerman, E. & Einav, S. Combating emerging viral threats. *Science* **348**, 282-283, doi:10.1126/science.aaa3778 (2015).

33 Raymonda, M. H. *et al.* Pharmacologic profiling reveals lapatinib as a novel antiviral against SARS-CoV-2 in vitro. *bioRxiv*, 2020.2011.2025.398859, doi:10.1101/2020.11.25.398859 (2020).

34 O'Donovan, S. M. *et al.* Identification of candidate repurposable drugs to combat COVID-19 using a signature-based approach. *Scientific Reports* **11**, 4495, doi:10.1038/s41598-021-84044-9 (2021).

35 Selvaraj, G., Kaliamurthi, S., Peslherbe, G. & Wei, D. Identifying potential drug targets and candidate drugs for COVID-19: biological networks and structural modeling approaches [version 1; peer review: 1 approved with reservations]. *F1000Research* **10**, doi:10.12688/f1000research.50850.1 (2021).

36 Mizutani, T., Fukushi, S., Saijo, M., Kurane, I. & Morikawa, S. Phosphorylation of p38 MAPK and its downstream targets in SARS coronavirus-infected cells. *Biochem Biophys Res Commun* **319**, 1228-1234, doi:10.1016/j.bbrc.2004.05.107 (2004).

37 Kindrachuk, J. *et al.* Antiviral Potential of ERK/MAPK and PI3K/AKT/mTOR Signaling Modulation for Middle East Respiratory Syndrome Coronavirus Infection as Identified by Temporal Kinome Analysis. *Antimicrobial agents and chemotherapy* **59**, 1088-1099, doi:10.1128/AAC.03659-14 (2015).

38 Venkataraman, T., Coleman, C. M. & Frieman, M. B. Overactive Epidermal Growth Factor Receptor Signaling Leads to Increased Fibrosis after Severe Acute Respiratory Syndrome Coronavirus Infection. *Journal of virology* **91**, e00182-00117, doi:10.1128/jvi.00182-17 (2017).

39 Bierman, A., Yerrapureddy, A., Reddy, N. M., Hassoun, P. M. & Reddy, S. P. Epidermal growth factor receptor (EGFR) regulates mechanical ventilation-induced lung injury in mice. *Transl Res* **152**, 265-272, doi:10.1016/j.trsl.2008.10.004 (2008).

40 Ishii, Y., Fujimoto, S. & Fukuda, T. Gefitinib prevents bleomycin-induced lung fibrosis in mice. *American journal of respiratory and critical care medicine* **174**, 550-556, doi:10.1164/rccm.200509-1534OC (2006).

41 Hardie, W. D. *et al.* EGF receptor tyrosine kinase inhibitors diminish transforming growth factor-α-induced pulmonary fibrosis. *American Journal of Physiology-Lung Cellular and Molecular Physiology* **294**, L1217-L1225, doi:10.1152/ajplung.00020.2008 (2008).

42 Freeman, M. C., Peek, C. T., Becker, M. M., Smith, E. C. & Denison, M. R. Coronaviruses Induce Entry-Independent, Continuous Macropinocytosis. *mBio* **5**, e01340-01314, doi:10.1128/mBio.01340-14 (2014).

43 Li, S.-W. *et al.* SARS coronavirus papain-like protease induces Egr-1-dependent up-regulation of TGF-β1 via ROS/p38 MAPK/STAT3 pathway. *Scientific Reports* **6**, 25754, doi:10.1038/srep25754 (2016).

44 Koka, V. *et al.* Angiotensin II up-regulates angiotensin I-converting enzyme (ACE), but down-regulates ACE2 via the AT1-ERK/p38 MAP kinase pathway. *The American journal of pathology* **172**, 1174-1183, doi:10.2353/ajpath.2008.070762 (2008).

45 Simões e Silva, A. C., Silveira, K. D., Ferreira, A. J. & Teixeira, M. M. ACE2, angiotensin-(1-7) and Mas receptor axis in inflammation and fibrosis. *Br J Pharmacol* **169**, 477-492, doi:10.1111/bph.12159 (2013).

46 Akhtar, S. *et al.* Transactivation of ErbB Family of Receptor Tyrosine Kinases Is Inhibited by Angiotensin-(1-7) via Its Mas Receptor. *PloS one* **10**, e0141657-e0141657, doi:10.1371/journal.pone.0141657 (2015).

47 Kuba, K. *et al.* A crucial role of angiotensin converting enzyme 2 (ACE2) in SARS coronavirus–induced lung injury. *Nature medicine* **11**, 875-879, doi:10.1038/nm1267 (2005).

48 Treon, S. P. *et al.* The BTK inhibitor ibrutinib may protect against pulmonary injury in COVID-19-infected patients. *Blood* **135**, 1912-1915, doi:10.1182/blood.2020006288 (2020).

49 Hudachek, S. F. & Gustafson, D. L. Physiologically based pharmacokinetic model of lapatinib developed in mice and scaled to humans. *Journal of pharmacokinetics and pharmacodynamics* **40**, 157-176, doi:10.1007/s10928-012-9295-8 (2013).

50 Neveu, G. *et al.* Identification and Targeting of an Interaction between a Tyrosine Motif within Hepatitis C Virus Core Protein and AP2M1 Essential for Viral Assembly. *PLoS pathogens* **8**, e1002845 (2012).

51 Bekerman, E. *et al.* Anticancer kinase inhibitors impair intracellular viral trafficking and exert broad-spectrum antiviral effects. *The Journal of clinical investigation* **127**, doi:10.1172/JCI89857 (2017).

52 Wang, P.-G., Tang, D.-J., Hua, Z., Wang, Z. & An, J. Sunitinib reduces the infection of SARS-CoV, MERS-CoV and SARS-CoV-2 partially by inhibiting AP2M1 phosphorylation. *Cell Discovery* **6**, 71, doi:10.1038/s41421-020-00217-2 (2020).

53 Ivens, T. *et al.* Development of a homogeneous screening assay for automated detection of antiviral agents active against severe acute respiratory syndrome-associated coronavirus. *Journal of virological methods* **129**, 56-63, doi:https://doi.org/10.1016/j.jviromet.2005.05.010 (2005).

54 Sun, C., Gardner, C. L., Watson, A. M., Ryman, K. D. & Klimstra, W. B. Stable, high-level expression of reporter proteins from improved alphavirus expression vectors to track replication and dissemination during encephalitic and arthritogenic disease. *Journal of virology* **88**, 2035-2046, doi:10.1128/JVI.02990-13 (2014).

55 Zou, G., Xu, H. Y., Qing, M., Wang, Q.-Y. & Shi, P.-Y. Development and characterization of a stable luciferase dengue virus for high-throughput screening. *Antiviral research* **91**, 11-19, doi:http://dx.doi.org/10.1016/j.antiviral.2011.05.001 (2011).

56 Johannessen, C. M. *et al.* COT drives resistance to RAF inhibition through MAP kinase pathway reactivation. *Nature* **468**, 968-972, doi:10.1038/nature09627 (2010).

57 Spiteri, G. *et al.* First cases of coronavirus disease 2019 (COVID-19) in the WHO European Region, 24 January to 21 February 2020. *Euro Surveill* **25**, doi:10.2807/1560-7917.Es.2020.25.9.2000178 (2020).

58 Case, J. B., Bailey, A. L., Kim, A. S., Chen, R. E. & Diamond, M. S. Growth, detection, quantification, and inactivation of SARS-CoV-2. *Virology* **548**, 39-48, doi:https://doi.org/10.1016/j.virol.2020.05.015 (2020).

59 Boudewijns, R. *et al.* STAT2 signaling as double-edged sword restricting viral dissemination but driving severe pneumonia in SARS-CoV-2 infected hamsters. *bioRxiv*, 2020.2004.2023.056838, doi:10.1101/2020.04.23.056838 (2020).

60 Sahoo, M. K. *et al.* Detection of Emerging Vaccine-Related Polioviruses by Deep Sequencing. *Journal of clinical microbiology* **55**, 2162-2171, doi:10.1128/jcm.00144-17 (2017).

61 Coutant, E. P. *et al.* Gram-scale synthesis of luciferins derived from coelenterazine and original insights into their bioluminescence properties. *Organic & biomolecular chemistry* **17**, 3709-3713, doi:10.1039/c9ob00459a (2019).

Acknowledgements

This work was supported by a gift from Frank Quattrone and Denise Foderaro (to SE), award number HDTRA11810039 from the Defense Threat Reduction Agency (DTRA)/Fundamental Research to Counter Weapons of Mass Destruction (to SE, SDJ and AN), award number W81XWH-16-1-0691 from the Department of Defense (DoD)/Congressionally Directed Medical Research Programs (CDMRP) (to SE and SDJ), and by the National Institutes for Health (NIH) grants 3R01DK107585-05S1 (to SD), UCOP-R00RG2642 (to SD and PG), and UCOP-R01RG3780 (to PG and DS). Flow cytometry analysis and IF confocal microscopy for this project were done on instruments in the Stanford Shared FACS Facility and Stanford Cell Science Imaging Facility (CSIF) respectively. We thank the Stanford SPARK program's advisors for critical advice and investigators who have provided plasmids (see Methods). We also thank the staff of Stanford Clinical Virology Laboratory for their help sequencing the SARS-CoV-2 USA-WA1/2020 isolate used in this work. Opinions, conclusions, interpretations, and recommendations are those of the authors and are not necessarily endorsed by the U.S. Army. The mention of trade names or commercial products does not constitute endorsement or recommendation for use by the Department of the Army or the Department of Defense.

Author Contributions

S.S., M.K, P.T.H, L.G., W.C., S.K, P.L., N.B, C.C., K.H, M.L. designed and performed the experiments and conducted data analysis. C.T., S.D., P.G., D.S.C, J.J., provided reagents and guidance. S.E., S.D.J., J.D., D.J., J.N, A.N, and B.A.P. provided scientific oversight and guidance. S.E, S.S., S.D.J, M.K. W.C, and D.J. wrote the first version of the manuscript. S.E., D.J., J.N., A.N., S.D.J. provided funding for the studies.

Competing interests

The authors declare no competing interests.

Figures

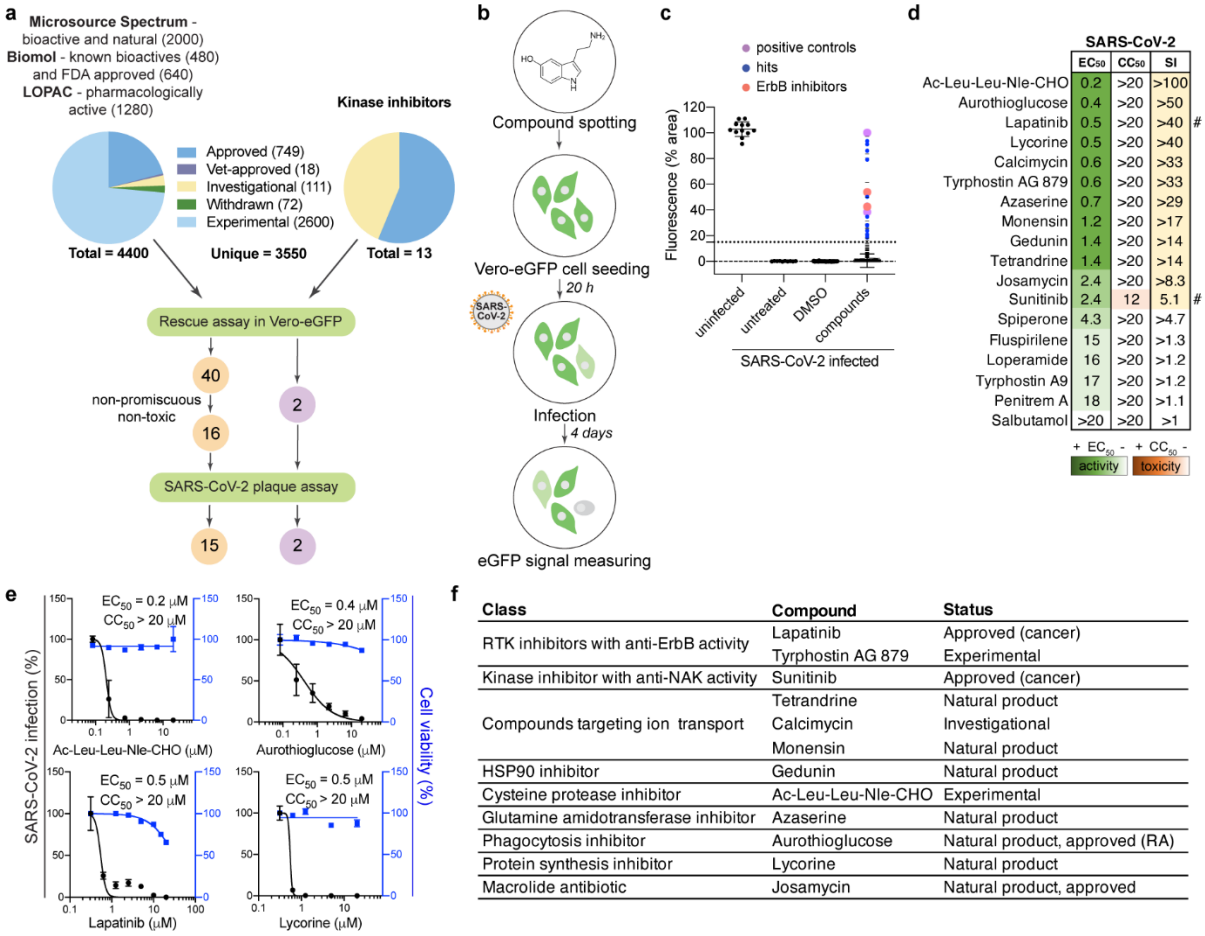

f

Class	Compound	Status
RTK inhibitors with anti-ErbB activity	Lapatinib	Approved (cancer)
	Tyrphostin AG 879	Experimental
Kinase inhibitor with anti-NAK activity	Sunitinib	Approved (cancer)
Compounds targeting ion transport	Tetrandrine	Natural product
	Calcimycin	Investigational
	Monensin	Natural product
HSP90 inhibitor	Gedunin	Natural product
Cysteine protease inhibitor	Ac-Leu-Leu-Nle-CHO	Experimental
Glutamine amidotransferase inhibitor	Azaserine	Natural product
Phagocytosis inhibitor	Aurothioglucose	Natural product, approved (RA)
Protein synthesis inhibitor	Lycorine	Natural product
Macrolide antibiotic	Josamycin	Natural product, approved

Figure 1. High-throughput screening (HTS) for compounds that counteract SARS-CoV-2-induced lethality and validation by plaque assays.
a, A Schematic of the screening and hit selection pipeline and the composition of the screened libraries. **b,** HTS assay schematic. Compounds were pre-spotted in 384-well plates at a final concentration of 10 μM. Next, Vero E6 cells constitutively expressing eGFP were added to each well and pre-incubated for 20 hours with the compounds, followed by SARS-CoV-2 infection (Belgium-GHB-03021, MOI = 0.001). eGFP signal measured at 4 days post-infection was used as an indicator for survival from viral-induced lethality. **c,** Boxplots of the percentage of fluorescence area values combining the entire HTS data set (two independent experiments) split into the four indicated categories. The box horizontal lines indicate the first, second (median), and third quartiles. Outliers above a cutoff of 15% were defined as positive hits. Dots represent individual compounds and colors denote positive controls (purple), new hits (blue), and ErbB inhibitors (peach). **d,** Heat map of the EC_{50} and CC_{50} values of hits emerging in the HTS color-coded based on the antiviral activity measured by plaque assays (green) and toxicity measured by alamarBlue assays (orange) 24 hours post-infection of Vero cells with SARS-CoV-2 (USA-WA1/2020 strain; MOI=0.05). Selectivity indices (SI) greater than 5 are depicted in yellow. # indicates compounds from the 13-kinase set that also protect from SARS-CoV-2 lethality in the HTS. **e,** Representative dose-response curves of hits depicting SARS-CoV-2 infection (black) and cell viability (blue). Data are relative to DMSO. **f,** The 12 most promising hit compounds emerging in the HTS.

Data in **panels d, e** are representative of 2 or more independent experiments. Individual experiments had 3 biological replicates. Shown are means ± SD. RA, Rheumatoid arthritis; RTK, receptor tyrosine kinase; NAK, NUMB-associated kinase.

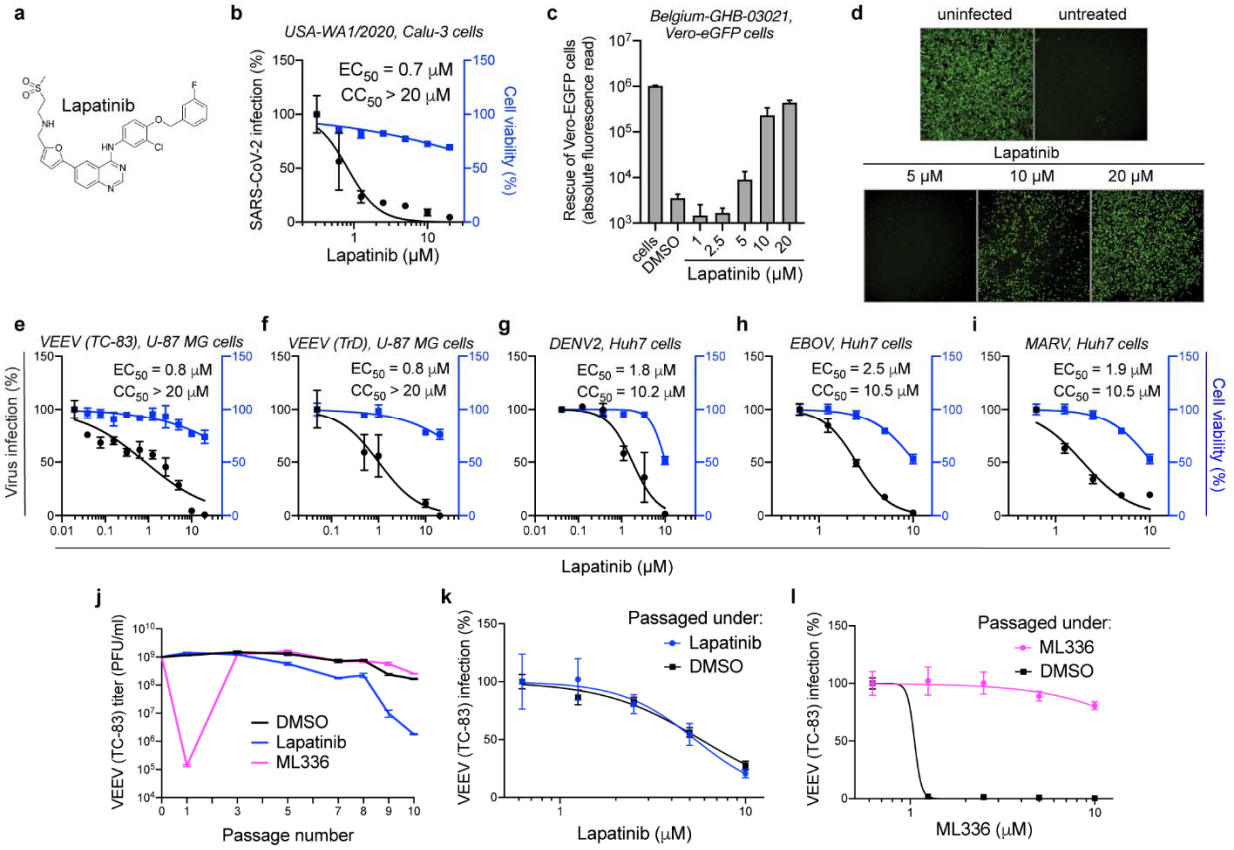

Figure 2. Lapatinib is a potent broad-spectrum antiviral with a high genetic barrier to resistance.

a, Chemical structure of lapatinib. **b,** Dose response to lapatinib of SARS-CoV-2 infection (black, USA-WA1/2020 strain; MOI=0.05) and cell viability (blue) in Calu-3 cells measured via plaque and alamarBlue assays at 24 hours post-infection, respectively. **c, d,** Dose-dependent graph **(c)** and corresponding florescence images **(d)** of Vero-eGFP cells rescued from SARS-CoV-2-induced lethality by lapatinib at 96 hours post-infection (Belgium-GHB-03021 strain; MOI=0.05). **e, f**, Dose response to lapatinib of infection with vaccine (TC-83) **(e)** and WT (Trinidad donkey (TrD)) **(f)** VEEV strains (MOI=0.1) in U-87 MG cells via plaque and alamarBlue assays at 24 hours post-infection, respectively. **g,** Dose response of DENV2 infection (blue) and cellular viability (black) to lapatinib measured in Huh7 cells via plaque and alamarBlue assays at 24 hours post-infection (MOI=0.1), respectively. **h, i** Dose response of EBOV (Kikwit isolate, MOI=1) **(h)** and MARV (Ci67 strain, MOI=2) **(i)** infections (blue) and cellular viability (black) to lapatinib measured in Huh7 cells 48 hours post-infection via microneutralization assay and CellTiter-Glo luminescent cell viability assay, respectively. **j,** VEEV (TC-83) was used to infect U-87 MG cells (MOI=0.1) and was then passaged every 24 hours by inoculation of naive U-87 MG cells with equal volumes of viral supernatants under DMSO treatment or selection with lapatinib or ML336 (VEEV nsP2 inhibitor) increasing from 2.5 to 15 μM over 10 passages. Viral titers were measured by plaque assays. **k, l,** Dose response to lapatinib **(k)** and ML336 **(l)** of VEEV (TC-83) harvested after 10 passages in U-87 MG cells in the presence of lapatinib **(k)** and ML336 **(l),** via luciferase assays. Data are representative of at least 2 experiments. All panels except J had 2 and 3 biological replicates. Means ± SD are shown. Data in **b**, **e-i, k** and **l** are relative to DMSO.

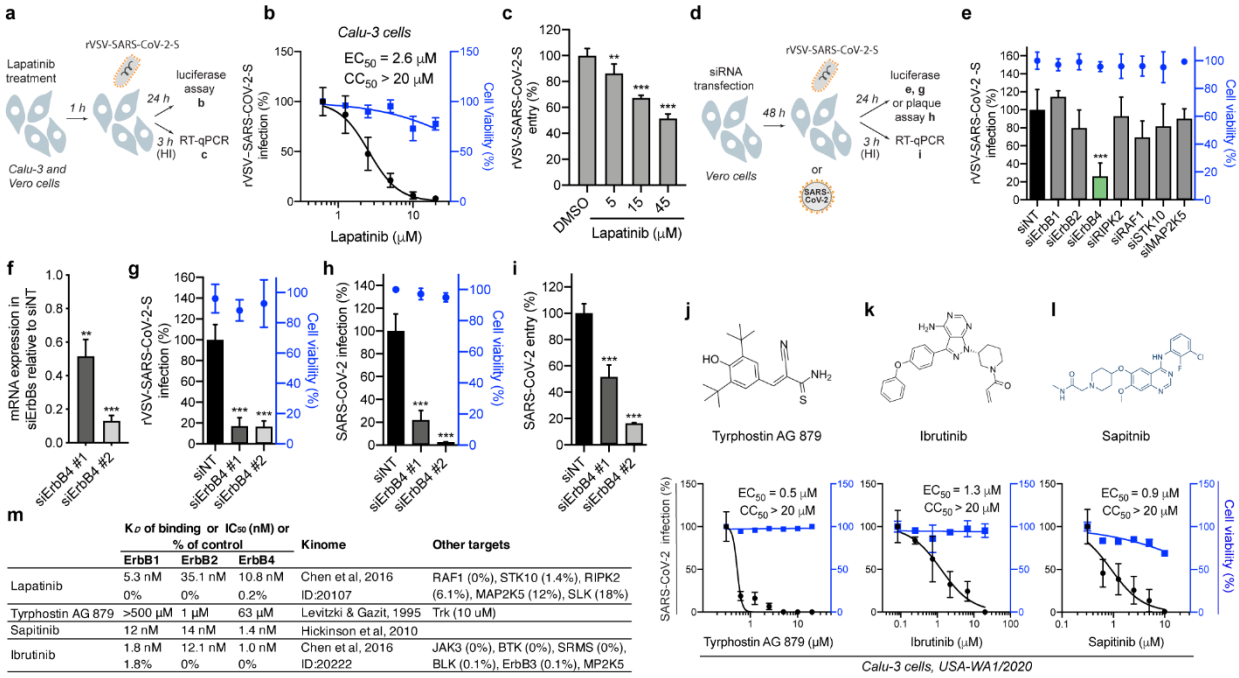

m

	K_D of binding or IC_{50} (nM) or % of control			Kinome	Other targets
	ErbB1	ErbB2	ErbB4		
Lapatinib	5.3 nM 0%	35.1 nM 0%	10.8 nM 0.2%	Chen et al, 2016 ID:20107	RAF1 (0%), STK10 (1.4%), RIPK2 (6.1%), MAP2K5 (12%), SLK (18%)
Tyrphostin AG 879	>500 μM	1 μM	63 μM	Levitzki & Gazit, 1995	Trk (10 uM)
Sapitinib	12 nM	14 nM	1.4 nM	Hickinson et al, 2010	
Ibrutinib	1.8 nM 1.8%	12.1 nM 0%	1.0 nM 0%	Chen et al, 2016 ID:20222	JAK3 (0%), BTK (0%), SRMS (0%), BLK (0.1%), ErbB3 (0.1%), MP2K5

Figure 3. ErbB4, but not other lapatinib's targets, is essential for SARS-CoV-2 entry. **a**, Schematic of the experiments shown in panels **b** and **c**. **b,** Dose response to lapatinib of rVSV-SARS-CoV-2-S infection (black) and cell viability (blue) in Calu-3 cells via luciferase and alamarBlue assays at 24 hours post-infection with a standard inoculum, respectively. **c,** Dose response to lapatinib of rVSV-SARS-CoV-2-S entry in Vero cells measured by RT-qPCR at 3 hours post-infection with a high inoculum (HI). **d,** Schematic of the experiments shown in panels **e, g, h, i. e,** rVSV-SARS-CoV-2-S infection by luciferase assays (black) and cell viability by alamarBlue assays (blue) measured at 24 hours post-infection of Vero cells transfected with the indicated siRNA pools. **f,** Confirmation of gene expression knockdown by RT-qPCR in Vero cells at 48 hours post-transfection. **g,** rVSV-SARS-CoV-2-S infection (MOI=0.1) measured by luciferase assays at 24 hours post-infection of Vero cells transfected with the indicated siRNAs, respectively. Shown in blue is cell viability by alamarBlue assays. **h,** SARS-CoV-2 infection at 24 hours post-infection of ErbB4-depleted Vero cells with SARS-CoV-2 (USA-WA1/2020 strain; MOI=0.05) measured by plaque assays. **i,** SARS-CoV-2 entry at 3 hours post-infection of Vero cells (MOI=1) measured by RT-qPCR. **j-l,** Chemical structures and dose response to tyrphostin AG 879 (**j**), ibrutinib (**k**) and sapitinib (**l**) of SARS-CoV-2 infection (black, USA-WA1/2020 strain; MOI=0.05) by plaque assays and cell viability (blue) by alamarBlue assays at 24 hours post-infection of Calu-3 cells. **m,** Binding affinity (K_D), enzymatic activity (IC_{50}) or percent binding of control (% control) of the indicated kinase inhibitors on the 3 catalytic ErbBs, the source of kinome data, and other targets these compounds bind and/or inhibit.
Data in all panels are representative of 2 or more independent experiments. Individual experiments had 3 biological replicates, means ± SD are shown. $^{**}P < 0.01$, $^{***}P < 0.001$ relative to DMSO (**b, c, j-l**) or to siNT **(e-i)** (one-way ANOVA followed by Dunnett's multiple comparisons test).

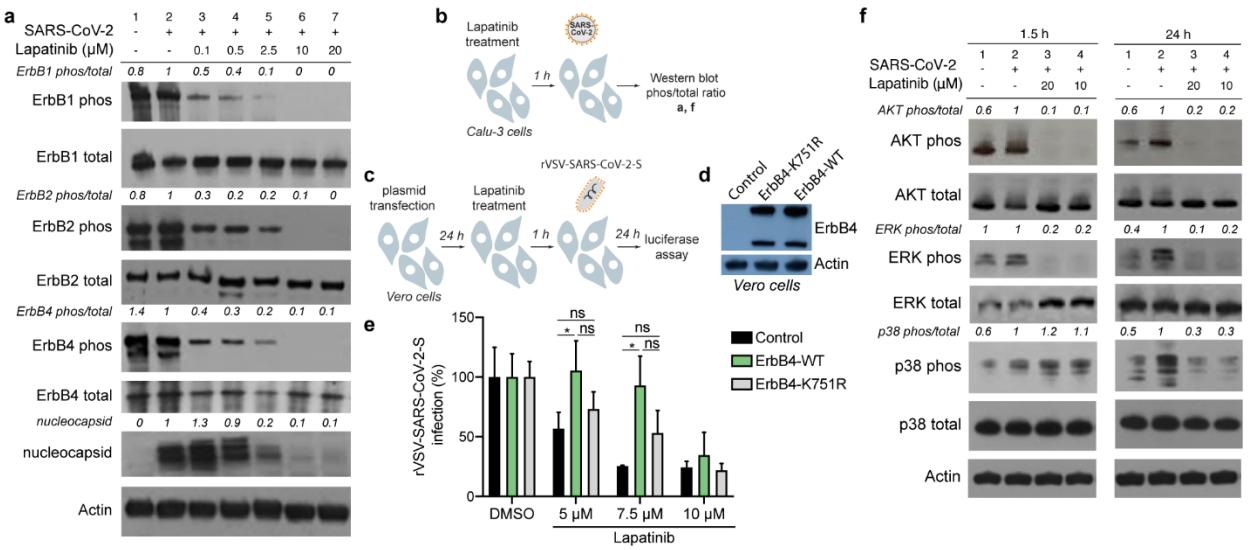

Figure 4. Lapatinib's antiviral activity is associated with functional inhibition of ErbB activity and downstream inflammatory and tissue injury signals and is mediated by ErbB4.

a, ErbB1, 2 and 4 phosphorylation in Calu-3 cells that are uninfected (lane 1), infected and treated with DMSO (lane 2) or infected and treated with increasing concentrations of lapatinib (lanes 3-7) measured by Western blotting 24 hours post-infection with SARS-CoV-2 (USA-WA1/2020 strain, MOI=1). **b,** Schematic of experiments shown in **a, f. c,** Schematic of the experiments shown in **d, e. d**, Level of ErbB4 and actin expression measured by Western blot following transfection of Vero cells with control or ErbB4-expressing plasmids. **e,** Rescue of rVSV-SARS-CoV-2-S infection in the presence of lapatinib upon ectopic expression of the indicated plasmids measured by luciferase assays 24 hours after infection in Vero cells. **f,** AKT, ERK, and p38 MAPK phosphorylation in Calu-3 cells that are uninfected (lane 1), infected and treated with DMSO (lane 2) or infected and treated with lapatinib (lanes 3 and 4) measured by Western blotting 1.5 hours and 24 hours post-infection with SARS-CoV-2 (USA-WA1/2020 strain, MOI=1). Shown are representative membranes blotted for phospho- and total proteins and quantitative phospho- to total protein ratio data relative to infected cells treated with DMSO (lane 2) (**a, f**). In panel **e** means±SD of results of two combined experiments conducted each with three replicates are shown. *P < 0.05 relative to DMSO by one-way ANOVA followed by Tukey's multiple comparisons test at each lapatinib concentration (**e**). Ns, non-significant.

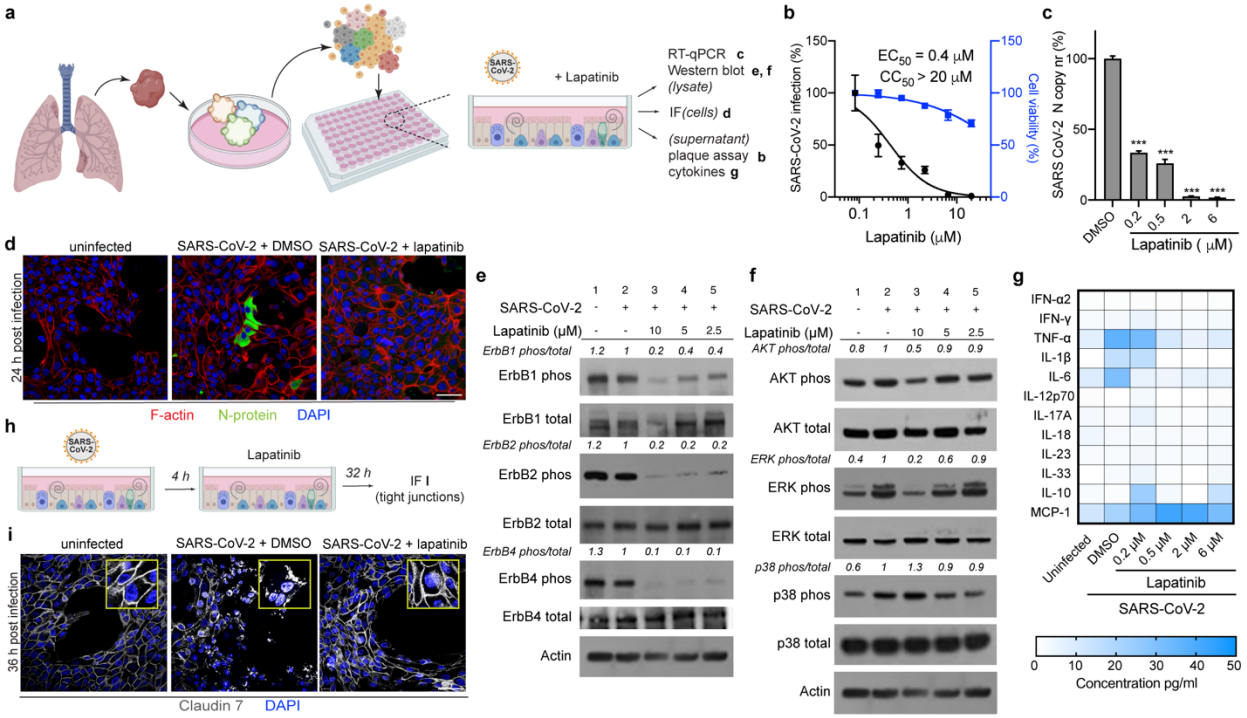

Fig. 5. Lapatinib inhibits SARS-CoV-2 infection, inflammation, and tissue injury *ex vivo* in human adult lung organoids (ALOs).

a, Schematic of the ALO model and the experimental procedures. ALOs were infected with virulent SARS-CoV-2 (USA-WA1/2020 strain, MOI=1). **b,** Dose response to lapatinib of SARS-CoV-2 infection (black) and cell viability (blue) in ALO supernatants measured via plaque and alamarBlue assays at 48 hours post-infection, respectively. **c**, Dose response to lapatinib of SARS-CoV-2 nucleocapsid (N) copy number in ALO lysates measured by RT-qPCR assays at 48 hours post-infection. **d,** Confocal IF microscopy images of F-actin (red), SARS-CoV-2 nucleocapsid (green) and DAPI (blue) in naïve and SARS-CoV-2-infected ALOs pre-treated with DMSO or 10 μM lapatinib 24 hours post-infection. **e, f,** Dose-dependent effect of lapatinib treatment on ErbB1, 2 and 4 (**e**) and AKT, ERK and p38 MAPK (**f**) phosphorylation in ALOs that are uninfected (lane 1), SARS-CoV-2-infected and treated with DMSO (lane 2) or infected and treated with lapatinib (lanes 3-5) measured by Western blotting 48 hours post-infection. Shown are representative membranes blotted for phospho- and total kinases and actin and quantitative phospho- to total kinase ratio data relative to infected ALOs treated with DMSO (lane 2). **g,** Heat map showing the concentration of cytokines (pg/mL) in the supernatants of ALOs under the indicated conditions at 48 hours post-infection with SARS-CoV-2 measured by LEGENDplex (Biolegend) kit. **h**, Schematic of the experiment shown in i. **i,** Confocal IF microscopy images of Claudin 7 (grey) and DAPI (blue) in naïve or SARS-CoV-2- infected ALOs treated at 4 hours post-infection either with DMSO or 10 μM lapatinib and imaged at 36 hours post-infection. Data in all panels are representative of 2 or more independent experiments. Individual experiments had 3 biological replicates, means ± SD are shown in panels **b** and **c**. Representative merged images at 40x magnification are shown in panels **d** and **i**. Scale bars are 50 μm. **P* < 0.05, ***P* < 0.01**,** ****P* < 0.001 relative to DMSO (**c**) (one-way ANOVA followed by Dunnett's multiple comparisons test).

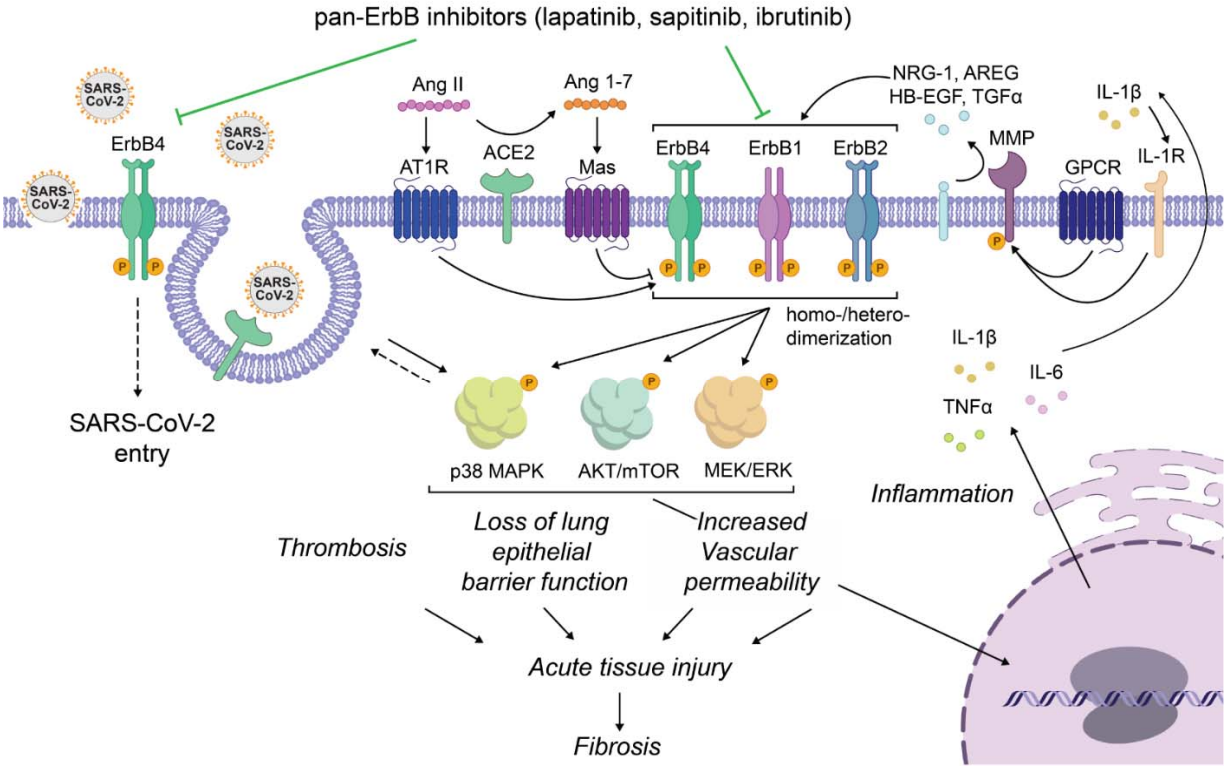

Fig. 6: Proposed model for the roles of ErbBs in the regulation of SARS-CoV-2 infection and pathogenesis and the mechanism of action of pan-ErbB inhibitors.
By inhibiting ErbB4, lapatinib suppresses SARS-CoV-2 entry. By inhibiting pan-ErbB activation by various ligands and unopposed Ang II effect, lapatinib inhibits activation of signaling pathways known to be activated and deleterious in severe pandemic coronaviral infections, thereby protecting from inflammation and tissue injury.

Extended data

This document includes:

1. Extended data figures and figure legends
2. Supplementary discussion
3. Extended data references

Extended data figures

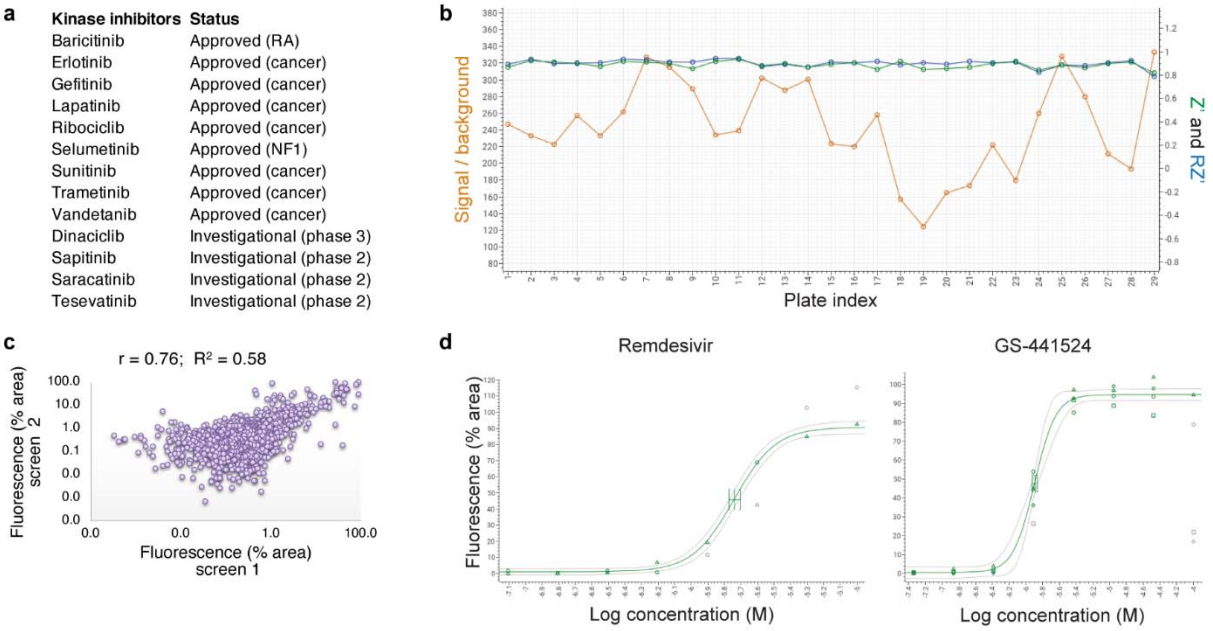

Extended data fig. 1: Characteristics and of the HTS.
a, The kinase inhibitors included in the self-assembled set. **b,** Quality control of each individual plate of the 29 screened by determination of the signal-to-background (S/B), and the Z' and RZ' values. All three parameters were measured for each 384-well screening plate using the virus control (infected, DMSO treated) and cell control (uninfected, untreated) wells. S/B values ranged from 124 – 333. Z' and RZ' values were > 0.78. Generally, S/B values >10 and (R)Z' values >0,5 are accepted as qualitative assays. All parameters were calculated using Genedata Screener. **c,** Scatter plot of the two replicate screens with a Pearson's correlation coefficient (*r*) of 0.76. **d**, Dose-dependent rescue of Vero-eGFP cells from SARS-CoV-2-induced lethality by remdesivir and its major metabolite, GS-441524, used as positive controls, 4 days post-infection with SARS-CoV-2 (Belgium-GHB-03021, MOI=0.001)

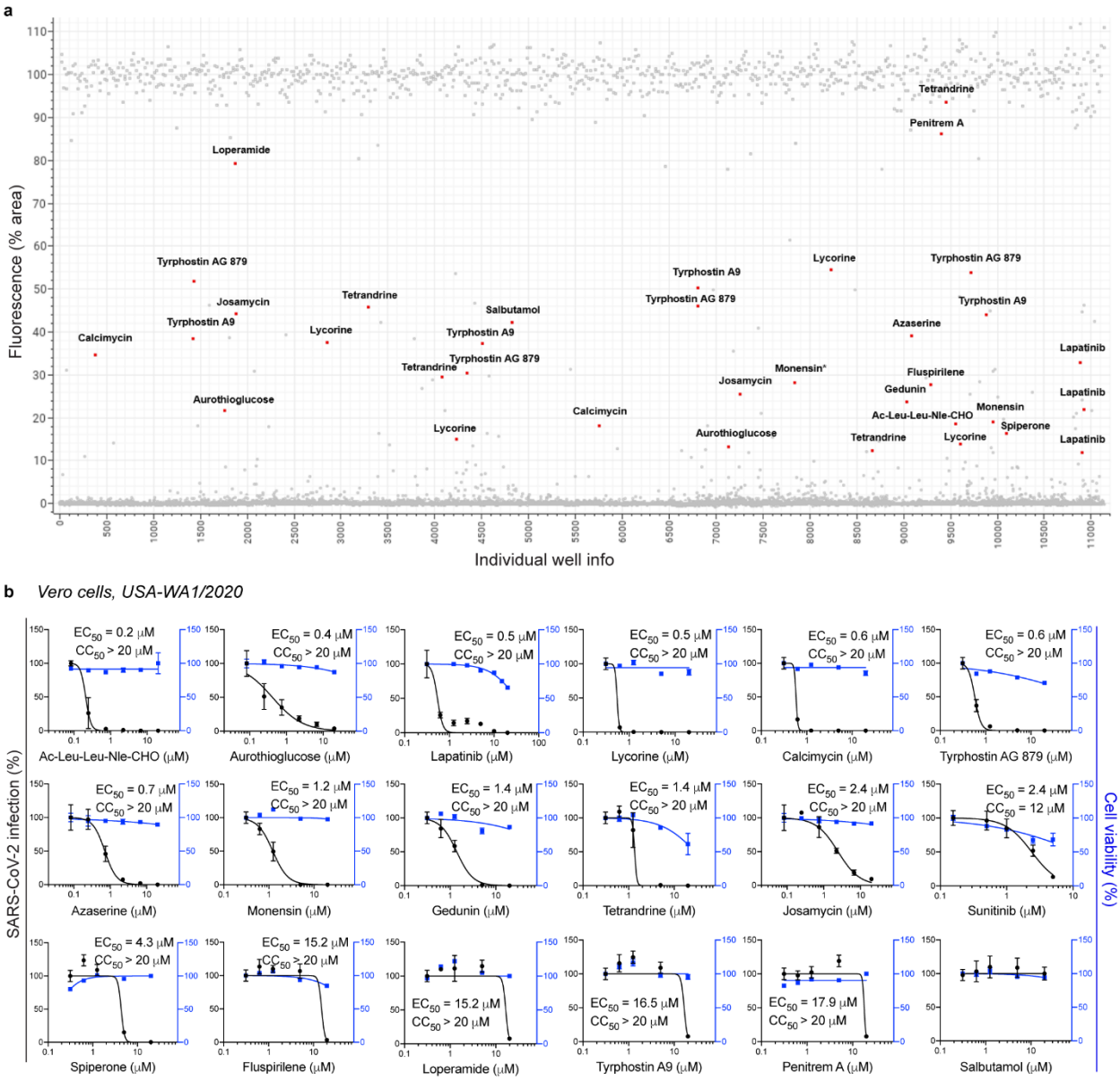

Extended data fig. 2: Hits emerging from the HTS.
a, Percentage of fluorescence area values from all wells including the virus controls (infected, DMSO treated) and the cell controls (uninfected, untreated) from the 29 384-well plates. The red dots depict hits emerging in the screening. Grey dots represent reference compounds such as nelfinavir, GS-441524 and compounds not prioritized for further analysis. **b,** Dose response curves to the indicated hits emerging from the HTS of SARS-CoV-2 infection (black, USA-WA1/2020 strain, MOI=0.05) and cell viability (blue) in Vero cells measured via plaque and alamarBlue assays at 24 hours post-infection, respectively.

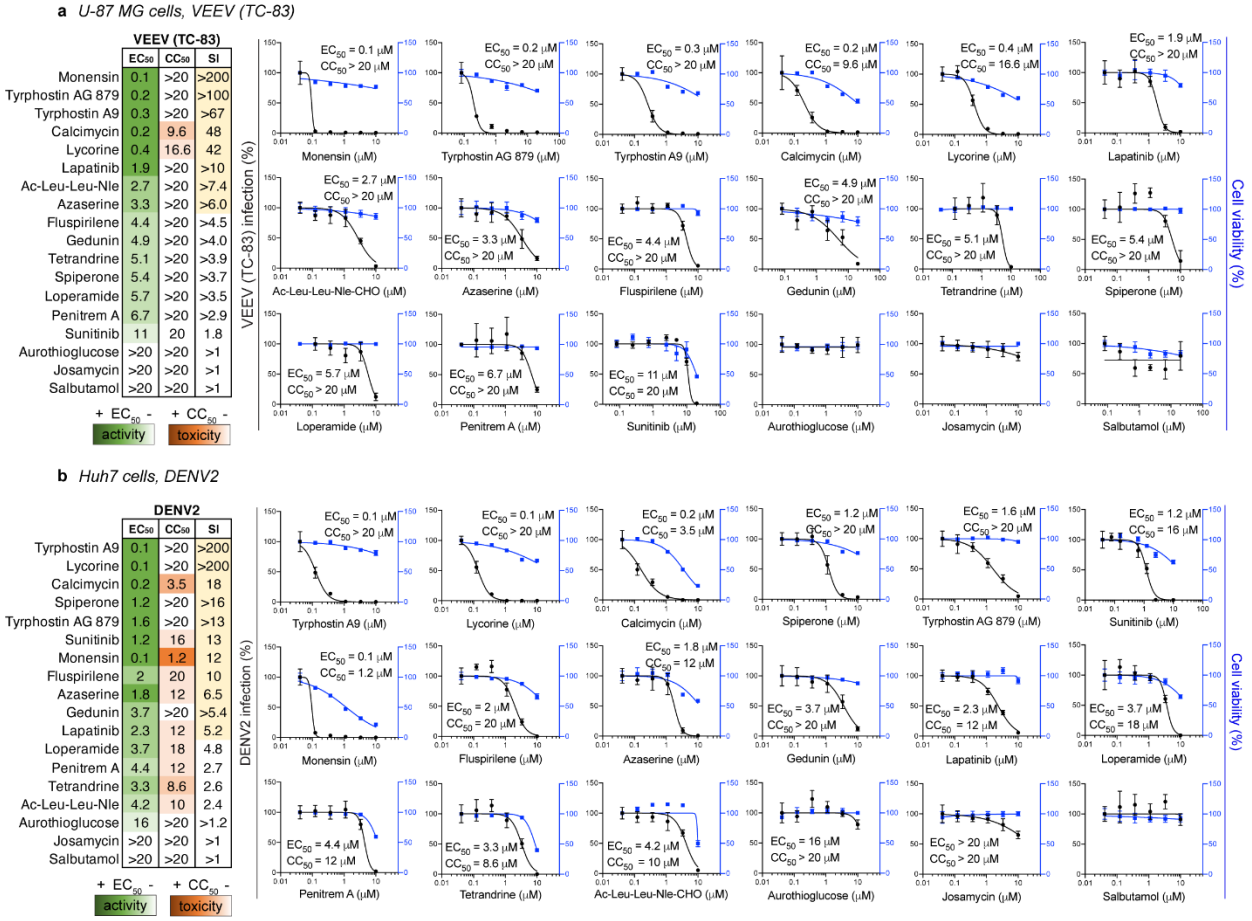

Extended data fig. 3: Broad-spectrum potential of hits and kinase inhibitor set.
a, b, The 18 compounds emerging from the HTS were tested for their effect on VEEV (TC-83) (**a**) and DENV2 (**b**) infections in U-87 MG and Huh7 cells, respectively, measured via luciferase assays, and for their effect on cell viability measured via alamarBlue assays. Left panels: Heat maps of the EC_{50} and CC_{50} values of the indicated compounds color-coded based on the antiviral activity (green) and toxicity (orange). Selectivity indices (SI) greater than 5 are depicted in yellow. Right panels: Dose response curves to the indicated compounds of VEEV (TC-83) (MOI=0.1) or DENV2 (MOI=0.05) infections (black) in U-87 MG and Huh7 cells, respectively, measured via luciferase assays and cell viability (blue) measured by alamarBlue assays at 24 hours post-infection.

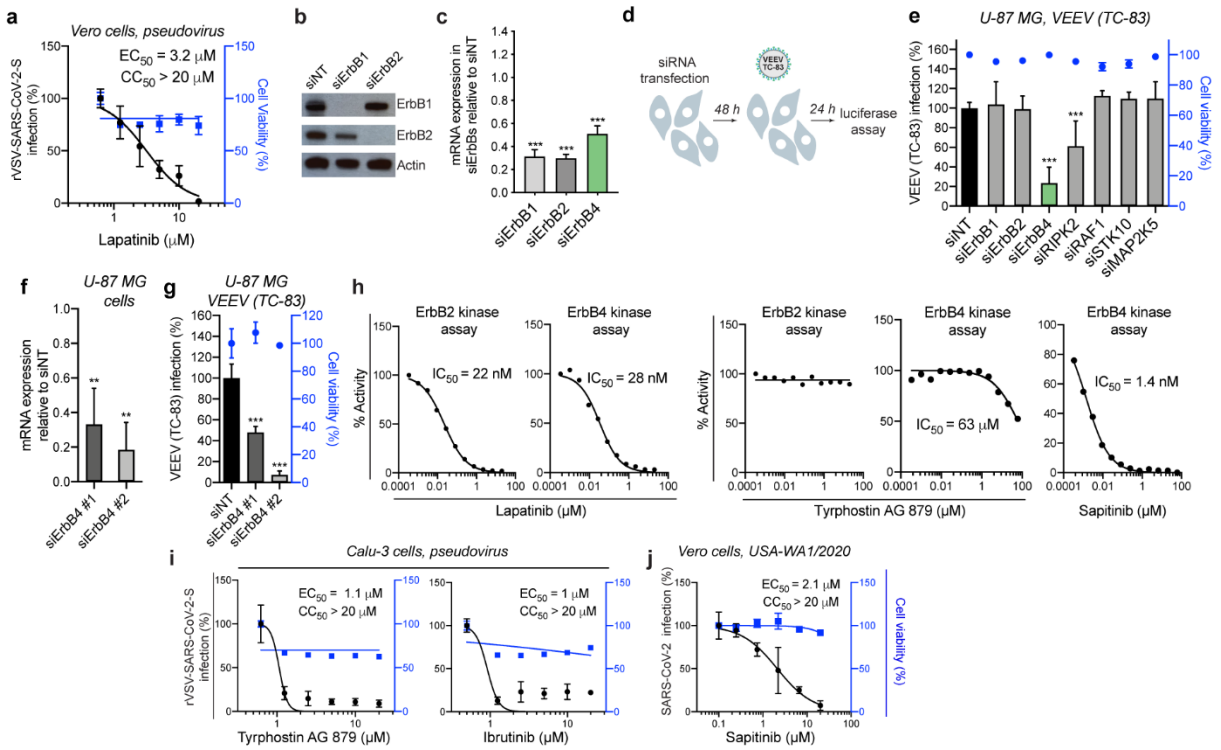

Extended data fig. 4: Validation of ErbB4 as an antiviral target.

a, Dose response to lapatinib of rVSV-SARS-CoV-2-S infection (black) and cell viability (blue) in Vero cells measured via luciferase and alamarBlue assays at 24 hours post-infection with a standard inoculum, respectively. **b,** Confirmation of siRNA-mediated gene expression knockdown by Western blot in Vero cells at 48 hours after transfection. Notably, two anti-ErbB4 antibodies detected no signal of endogenous protein in Vero cells in two independent experiments. **c,** Confirmation of siRNA-mediated (ON-TARGETplus SMARTpool siRNAs (Dharmacon)) gene expression knockdown by RT-qPCR in Vero cells. Shown is gene expression normalized to GAPDH and expressed relative to the respective gene level in the non-target (siNT) control at 48 hours post-transfection. **d,** Schematic of the experiments shown in panels **e-g**. **e,** VEEV (T-83) infection by luciferase assays and cell viability by alamarBlue assays (blue) measured at 24 hours post-infection of U-87 MG cells transfected with the indicated siRNA pools (MOI=0.1). **f,** Confirmation of gene expression knockdown by RT-qPCR in U-87 MG cells at 48 hours post-transfection. **g,** VEEV (T-83) infection (MOI=0.1) measured by luciferase assays at 24 hours post-infection of U-87 MG cells transfected with the indicated siRNAs. Shown in blue is cell viability by alamarBlue assays. **h,** Dose response to lapatinib, tyrphostin AG 879 and sapitinib of ErbB2 and/or ErbB4 kinase activity *in vitro* (Nanosyn). **i,** Dose response to tyrphostin AG 879 and ibrutinib of rVSV-SARS-CoV-2-S infection (black) by luciferase assays and cell viability (blue) by alamarBlue assays at 24 hours post-infection of Calu-3 cells. **j,** Dose response to sapitinib of SARS-CoV-2 infection (black) by plaque assay and cell viability (blue) by alamarBlue assay 24 hours post-infection of Vero cells.
Data in panels **a-g, i, j** are representative of 2 or more independent experiments. Individual experiments had 3 biological replicates, means ± SD are shown. * $^{**}P < 0.01$, $^{***}P < 0.001$ relative to siNT by one-way ANOVA followed by Dunnett's multiple comparisons test.

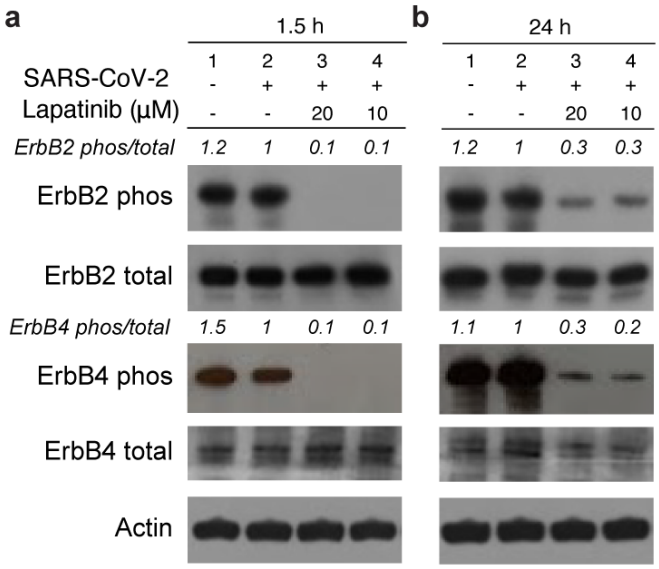

Extended data fig. 5: Lapatinib treatment modulates ErbBs.
a, b, ErbB2 and ErbB4 phosphorylation in Calu-3 cells that are uninfected (lane 1), infected and treated with DMSO (lane 2) or infected and treated with lapatinib (lanes 3 and 4) measured by Western blotting 1.5 hours (**a**) and 24 hours (**b**) post-infection with SARS-CoV-2 (USA-WA1/2020 strain**,** MOI=1). Shown are representative membranes blotted for phospho- and total ErbB2, ErbB4, and actin and quantitative phospho- to total ErbB ratio data relative to infected cells treated with DMSO (lane 2).

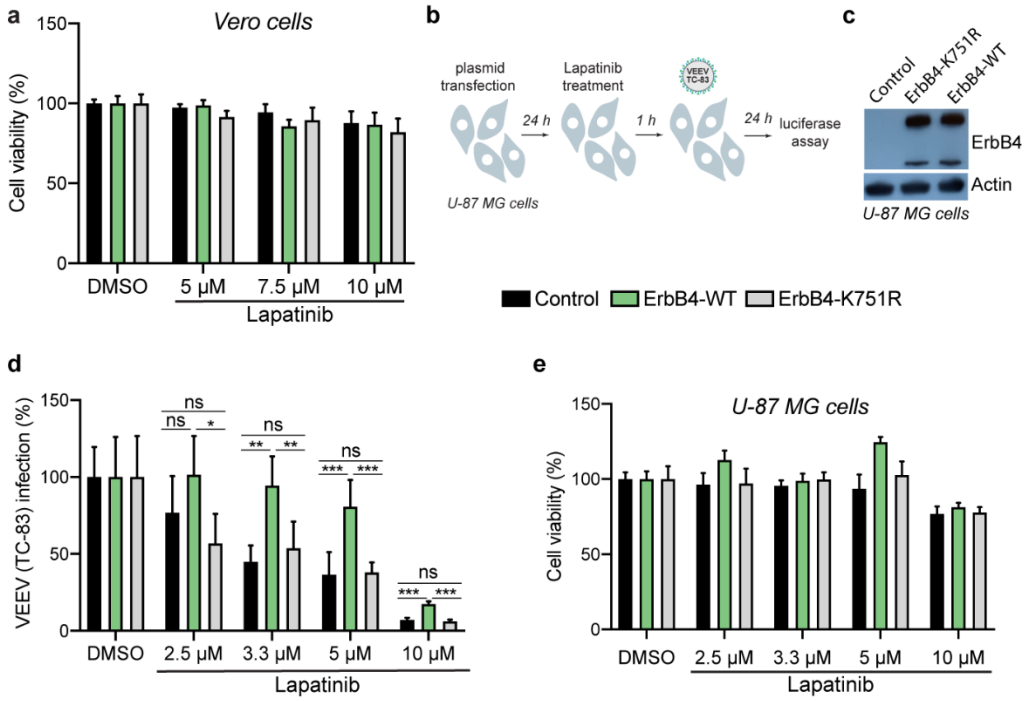

Extended data fig. 6: ErbB4 is a molecular target mediating lapatinib's antiviral effect. **a,** Vero cell viability measured by alamarBlue assays 48 hours post-transfection of the indicated plasmids. Data relative to the respective DMSO controls are shown. **b,** Schematics of the experiments shown in **c-e.** **c,** Level of ErbB4 and actin expression measured by Western blot following transfection of U-87 MG cells with control or ErbB4-expressing plasmids. **d,** Rescue of VEEV (TC-83) infection in the presence of lapatinib upon ectopic expression of the indicated plasmids measured by luciferase assays 24 hours after infection. **e,** U-87 MG cell viability measured by alamarBlue assays 48 hours post-transfection of the indicated plasmids. Data relative to the respective DMSO controls are shown. Shown in panels **a, d**, **e** are means±SD of results of two combined experiments conducted each with three (**a**) or five (d**, e**) replicates. **P* < 0.05, ***P* < 0.01 **,** ****P* < 0.001 relative to DMSO by 1-way ANOVA with Tukey's multiple comparisons test at each lapatinib concentration. Ns, non-significant.

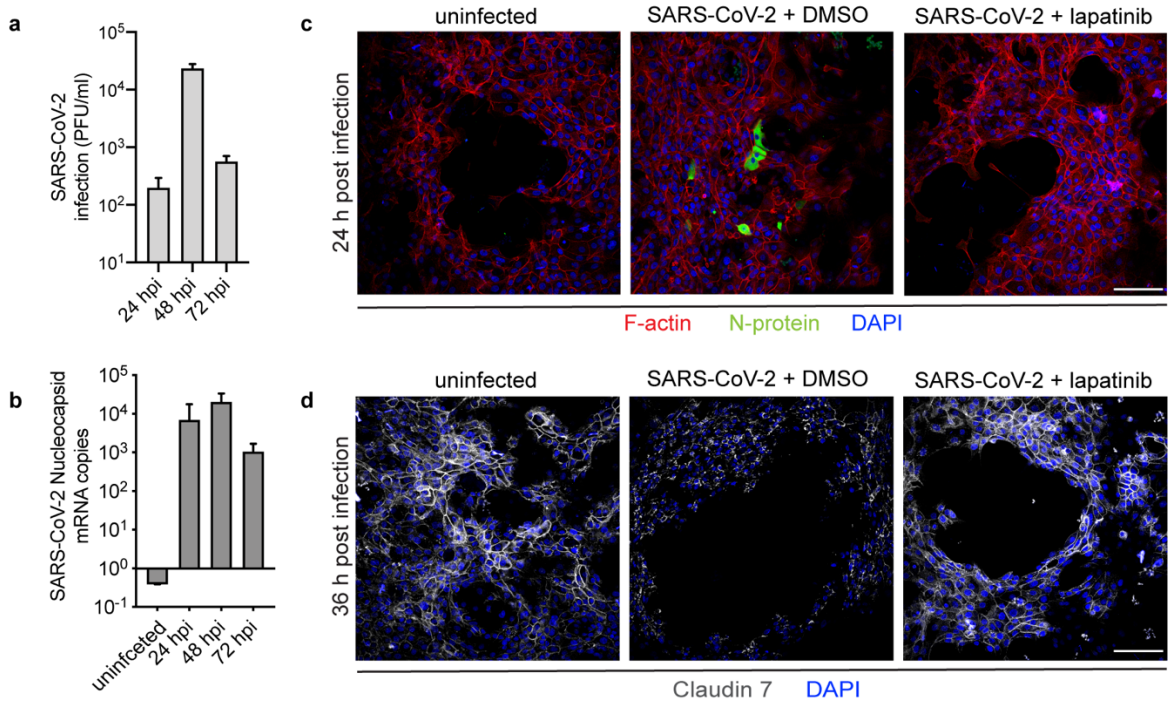

Extended data fig. 7: Human ALOs for studying the antiviral and tissue protective effects of lapatinib.

a, b, Viral titer by plaque assays in culture supernatants (**a**) and viral nucleocapsid (N) copy number analyzed by RT-qPCR in lysates (**b**) from human lung organoids at 24, 48 and 72 hours post-infection. **c,** Confocal IF microscopy images of F-actin (red), SARS-CoV-2 nucleocapsid (green) and DAPI (blue) in naïve and SARS-CoV-2-infected ALOs pre-treated with DMSO or 10 µM lapatinib 24 hours post-infection. **d,** Confocal IF microscopy images of Claudin 7 (grey) and DAPI (blue) in naïve or SARS-CoV-2- infected ALOs treated at 4 hours post-infection either with DMSO or 10 µM lapatinib and imaged at 36 hours post-infection. Representative merged images at 20x magnification are shown in panels **c** and **d**. Scale bars are 100 µm.

Supplementary discussion

Safety considerations and drug-drug interactions of lapatinib

Although toxicity is a concern when targeting host functions, lapatinib has a favorable safety profile, particularly when used as a monotherapy and for short durations, as those required to treat acute infections.

Notably, lapatinib's safety profile in the package insert was based on data from over 12,000 patients with advanced cancer who received lapatinib in combination with capecitabine or trastuzumab plus an aromatase inhibitor and for long durations[1-3]. As monotherapy, lapatinib was tested in several open-label studies with a median duration of 7-28 weeks in patients with advanced cancer[4-11]. The most common adverse events attributed to lapatinib were diarrhea, rash, nausea, pruritus, and fatigue, with diarrhea being the most common adverse event resulting in drug discontinuation. The most common laboratory abnormalities with combination therapy were increased liver function tests, which were infrequently severe[1-3,12]. More severe adverse events including transient, reversible decreases in left ventricular ejection fraction, prolongation of QT interval, and hepatotoxicity, were also documented, yet infrequently, and with the exception of cardiac toxicity, primarily in patients receiving lapatinib in combination treatment[1,10,13,14].

Notably, unlike erlotinib and gefitinib, lapatinib monotherapy has not been associated with pneumonitis, interstitial lung disease or lung fibrosis[4-11]. The estimated incidence of 0.2% for these adverse effects is based on patients receiving lapatinib in combination with other drugs[15-20] known to cause pneumonitis and/or lung fibrosis[21-23], and sometimes also with radiation, for a median duration of 24-45 weeks. We predict that lapatinib's distinct off-target profile accounts for this difference in the occurrence of these adverse events. Indeed, cyclin G-associated kinase (GAK), an off-target of erlotinib (K_D=3.1 nM, IC_{50}=0.88 µM) and gefitinib (K_D=6.5 nM, IC_{50}=0.41 µM), but not of lapatinib (K_D=980 nM, IC_{50}>5 µM)[24], has been implicated in pulmonary alveolar function and stem cell regeneration, and its inhibition is thought to be the mechanism underlying gefinitib- and erlotinib- induced lung toxicity[25,26].

An important consideration with lapatinib is, however, its potential for drug-drug interactions. Since metabolized by CYP3A4, concurrent use of suppressors of CYP3A4 should be avoided to reduce risk of QT prolongation. Concurrent treatment with CYP3A4 inducers should also be avoided, as this can reduce lapatinib's levels to sub-therapeutic. Of particular relevance is the CYP3A4 inducer dexamethasone used as standard of care for moderate COVID-19 patients. Since other steroids do not induce CYP3A4, lapatinib could be studied in combination with hydrocortisone or prednisone, which have been shown to comparably protect COVID-19 patients[27-29].

Other hits emerging in the screen

Another approved anticancer drug that emerged in the HTS was sunitinib, a multi-kinase inhibitor that we have shown to protect mice from DENV and EBOV challenges when given in combination with erlotinib by inhibiting NAK-mediated intracellular viral trafficking[30-32]. Sunitinib was recently shown to suppress pan-corona pseudotyped viral infections[33]. AG 879, another kinase inhibitor demonstrating anti-SARS-CoV-2 activity, was reported to suppress replication of multiple viruses including a mouse hepatitis virus (Coronaviridae) in cultured cells and to protect mice from influenza A virus (IAV) challenge[34-36]. Nevertheless, since we could not confirm its anti-ErbB activity, the precise target(s) mediating the antiviral effect remain to be elucidated.

Ion transport across cell membranes is another function that emerged in our HTS as a candidate target for anti-SARS-CoV-2 approaches. Among the hits was tetrandine, a calcium channel blocker with anti-inflammatory and anti-fibrogenic properties used as a medicinal herb for the treatment of lung silicosis, liver cirrhosis, and rheumatoid arthritis[37]. Tetrandine was previously shown to inhibit EBOV entry in cultured cells and protect EBOV-infected mice by inhibiting endosomal calcium channels[38]. Monensin, an antiprotozoal agent, and calcimycin, shown to inhibit VSV and IAV infections[39,40], are both ionophores that facilitate the transport of sodium/potassium and calcium across the membrane, respectively. Spiperone, an activator of chloride channels licensed in Japan for the treatment of schizophrenia, was another hit.

The emergence of gedunin, a natural product that inhibits HSP90 and has anti-inflammatory properties, suggests a potential role for HSP90 in SARS-CoV-2 infection, as in other viral infections[41,42]. Lycorine, a protein synthesis inhibitor[43] was also shown to suppress replication of multiple viruses including SARS-CoV in cultured cells[44-47] and mortality of mice infected with human enterovirus 71[48]. The underlying mechanism of action in influenza was thought to be inhibition of export of viral ribonucleoprotein complexes from the nucleus[44], yet lycorine also exhibits anti-inflammatory effects[49]. Azaserine is a natural serine derivative that irreversibly inhibits γ-glutamyltransferase in the metabolic hexosamine pathway. Independently of this target, it was shown to protect from endothelial cell inflammation and injury[50].

Aurothioglucose has been used for the treatment of rheumatoid arthritis and is thought to inhibit the activity of adenylyl cyclase in inflammatory pathways[51]. Ac-Leu-Leu-Nle-CHO is used as a research tool to inhibit calpain 1 and 2 (CAPN1 and 2)[52], cysteine proteases required for SARS-CoV[53], echovirus 1[54] and herpes simplex virus[55] infections. Targeting calpain proteases was shown to inhibit SARS-CoV-2[56], SARS-CoV[57] and IAV replication[58] and to exert anti-inflammatory and tissue protective effects[59,60] including in a reovirus-induced myocarditis mouse model[61]. Beyond their host-targeted effects, Ac-Leu-Leu-Nle-CHO and aurothioglucose may have direct antiviral effects against the SARS-CoV-2 M^{pro} or 3C-like proteases, respectively[56,62]. Lastly, josamycin is a natural macrolide antibiotic with an anti-inflammatory activity used in humans in Europe and Japan. Other macrolides have shown anti-IAV and anti-inflammatory activities[63]. These findings reveal candidate targets for anti-SARS-CoV-2 approaches. Moreover, they underscore the potential utility of natural products as broad-spectrum antivirals, yet limited scalability typically challenges the use of these products.

Extended data references

1 Novartis. Tykerb (U.S. package insert). (2018).

2 Pivot, X. *et al.* CEREBEL (EGF111438): A Phase III, Randomized, Open-Label Study of Lapatinib Plus Capecitabine Versus Trastuzumab Plus Capecitabine in Patients With Human Epidermal Growth Factor Receptor 2-Positive Metastatic Breast Cancer. *J Clin Oncol* **33**, 1564-1573, doi:10.1200/jco.2014.57.1794 (2015).

3 Schwartzberg, L. S. *et al.* Lapatinib plus letrozole as first-line therapy for HER-2+ hormone receptor-positive metastatic breast cancer. *The oncologist* **15**, 122-129, doi:10.1634/theoncologist.2009-0240 (2010).

4 Blackwell, K. L. *et al.* Single-agent lapatinib for HER2-overexpressing advanced or metastatic breast cancer that progressed on first- or second-line trastuzumab-containing regimens. *Ann Oncol* **20**, 1026-1031, doi:10.1093/annonc/mdn759 (2009).

5 Blackwell, K. L. *et al.* Randomized study of Lapatinib alone or in combination with trastuzumab in women with ErbB2-positive, trastuzumab-refractory metastatic breast cancer. *J Clin Oncol* **28**, 1124-1130, doi:10.1200/jco.2008.21.4437 (2010).

6 Burris, H. A., 3rd *et al.* Phase I safety, pharmacokinetics, and clinical activity study of lapatinib (GW572016), a reversible dual inhibitor of epidermal growth factor receptor tyrosine kinases, in heavily pretreated patients with metastatic carcinomas. *J Clin Oncol* **23**, 5305-5313, doi:10.1200/jco.2005.16.584 (2005).

7 Burstein, H. J. *et al.* A phase II study of lapatinib monotherapy in chemotherapy-refractory HER2-positive and HER2-negative advanced or metastatic breast cancer. *Ann Oncol* **19**, 1068-1074, doi:10.1093/annonc/mdm601 (2008).

8 Gomez, H. L. *et al.* Efficacy and Safety of Lapatinib As First-Line Therapy for ErbB2-Amplified Locally Advanced or Metastatic Breast Cancer. *Journal of Clinical Oncology* **26**, 2999-3005, doi:10.1200/jco.2007.14.0590 (2008).

9 Hurvitz, S. A. & Kakkar, R. Role of lapatinib alone or in combination in the treatment of HER2-positive breast cancer. *Breast Cancer (Dove Med Press)* **4**, 35-51, doi:10.2147/BCTT.S29996 (2012).

10 Perez, E. A. *et al.* Cardiac safety of lapatinib: pooled analysis of 3689 patients enrolled in clinical trials. *Mayo Clinic proceedings* **83**, 679-686, doi:10.4065/83.6.679 (2008).

11 Toi, M. *et al.* Lapatinib monotherapy in patients with relapsed, advanced, or metastatic breast cancer: efficacy, safety, and biomarker results from Japanese patients phase II studies. *British journal of cancer* **101**, 1676-1682, doi:10.1038/sj.bjc.6605343 (2009).

12 Piccart-Gebhart, M. *et al.* Adjuvant Lapatinib and Trastuzumab for Early Human Epidermal Growth Factor Receptor 2-Positive Breast Cancer: Results From the

Randomized Phase III Adjuvant Lapatinib and/or Trastuzumab Treatment Optimization Trial. *J Clin Oncol* **34**, 1034-1042, doi:10.1200/jco.2015.62.1797 (2016).

13 Kloth, J. S. L. *et al.* Incidence and relevance of QTc-interval prolongation caused by tyrosine kinase inhibitors. *British journal of cancer* **112**, 1011-1016, doi:10.1038/bjc.2015.82 (2015).

14 Dogan, E. *et al.* Evaluation of cardiac safety of lapatinib therapy for ErbB2-positive metastatic breast cancer: a single center experience. *Medical oncology (Northwood, London, England)* **29**, 3232-3239, doi:10.1007/s12032-012-0253-5 (2012).

15 Hackshaw, M. D. *et al.* Incidence of pneumonitis/interstitial lung disease induced by HER2-targeting therapy for HER2-positive metastatic breast cancer. *Breast cancer research and treatment* **183**, 23-39, doi:10.1007/s10549-020-05754-8 (2020).

16 Jagiello-Gruszfeld, A. *et al.* A single-arm phase II trial of first-line paclitaxel in combination with lapatinib in HER2-overexpressing metastatic breast cancer. *Oncology* **79**, 129-135, doi:10.1159/000318043 (2010).

17 Capri, G. *et al.* An open-label expanded access study of lapatinib and capecitabine in patients with HER2-overexpressing locally advanced or metastatic breast cancer. *Ann Oncol* **21**, 474-480, doi:10.1093/annonc/mdp373 (2010).

18 Xu, B.-H. *et al.* Lapatinib plus capecitabine in treating HER2-positive advanced breast cancer: efficacy, safety, and biomarker results from Chinese patients. *Chin J Cancer* **30**, 327-335, doi:10.5732/cjc.010.10507 (2011).

19 Bates, C. A. *et al.*

20 Brenner, T. *et al.* Rapid-Onset Acute Respiratory Distress Syndrome (ARDS) in a Patient Undergoing Metastatic Liver Resection: A Case Report and Review of the Literature. *Anesthesiol Res Pract* **2010**, 586425, doi:10.1155/2010/586425 (2010).

21 Chan, A. K., Choo, B. A. & Glaholm, J. Pulmonary toxicity with oxaliplatin and capecitabine/5-Fluorouracil chemotherapy: a case report and review of the literature. *Onkologie* **34**, 443-446, doi:10.1159/000331133 (2011).

22 Torrisi, J. M. *et al.* CT findings of chemotherapy-induced toxicity: what radiologists need to know about the clinical and radiologic manifestations of chemotherapy toxicity. *Radiology* **258**, 41-56, doi:10.1148/radiol.10092129 (2011).

23 Bielopolski, D. *et al.* Paclitaxel-induced pneumonitis in patients with breast cancer: case series and review of the literature. *Journal of chemotherapy (Florence, Italy)* **29**, 113-117, doi:10.1179/1973947815y.0000000029 (2017).

24 Asquith, C. R. M. *et al.* Design and Analysis of the 4-Anilinoquin(az)oline Kinase Inhibition Profiles of GAK/SLK/STK10 Using Quantitative Structure-Activity Relationships. *ChemMedChem* **15**, 26-49, doi:10.1002/cmdc.201900521 (2020).

25 Tabara, H. *et al.* Neonatal lethality in knockout mice expressing the kinase-dead form of the gefitinib target GAK is caused by pulmonary dysfunction. *PLoS One* **6**, e26034, doi:10.1371/journal.pone.0026034 (2011).

26 Bates, C. A. *et al.* in *A61. EPITHELIAL BIOLOGY American Thoracic Society International Conference Abstracts* A2125-A2125 (American Thoracic Society, 2019).

27 Group, T. W. R. E. A. f. C.-T. W. Association Between Administration of Systemic Corticosteroids and Mortality Among Critically Ill Patients With COVID-19: A Meta-analysis. *JAMA* **324**, 1330-1341, doi:10.1001/jama.2020.17023 (2020).

28 Dequin, P.-F. *et al.* Effect of Hydrocortisone on 21-Day Mortality or Respiratory Support Among Critically Ill Patients With COVID-19: A Randomized Clinical Trial. *JAMA* **324**, 1298-1306, doi:10.1001/jama.2020.16761 (2020).

29 Investigators, T. W. C. f. t. R.-C. Effect of Hydrocortisone on Mortality and Organ Support in Patients With Severe COVID-19: The REMAP-CAP COVID-19 Corticosteroid Domain Randomized Clinical Trial. *JAMA* **324**, 1317-1329, doi:10.1001/jama.2020.17022 (2020).

30 Neveu, G. *et al.* Identification and Targeting of an Interaction between a Tyrosine Motif within Hepatitis C Virus Core Protein and AP2M1 Essential for Viral Assembly. *PLoS pathogens* **8**, e1002845 (2012).

31 Bekerman, E. *et al.* Anticancer kinase inhibitors impair intracellular viral trafficking and exert broad-spectrum antiviral effects. *The Journal of clinical investigation* **127**, doi:10.1172/JCI89857 (2017).

32 Pu, S. *et al.* BIKE regulates dengue virus infection and is a cellular target for broad-spectrum antivirals. *Antiviral Res* **184**, 104966, doi:10.1016/j.antiviral.2020.104966 (2020).

33 Wang, P.-G., Tang, D.-J., Hua, Z., Wang, Z. & An, J. Sunitinib reduces the infection of SARS-CoV, MERS-CoV and SARS-CoV-2 partially by inhibiting AP2M1 phosphorylation. *Cell Discovery* **6**, 71, doi:10.1038/s41421-020-00217-2 (2020).

34 Kumar, N., Liang, Y., Parslow, T. G. & Liang, Y. Receptor Tyrosine Kinase Inhibitors Block Multiple Steps of Influenza A Virus Replication. *Journal of virology* **85**, 2818-2827, doi:10.1128/jvi.01969-10 (2011).

35 Kumar, N., Sharma, N. R., Ly, H., Parslow, T. G. & Liang, Y. Receptor tyrosine kinase inhibitors that block replication of influenza a and other viruses. *Antimicrobial agents and chemotherapy* **55**, 5553-5559, doi:10.1128/AAC.00725-11 (2011).

36 Zoeller, R. A. & Geoghegan-Barek, K. A cell-based high-throughput screen identifies tyrphostin AG 879 as an inhibitor of animal cell phospholipid and fatty acid biosynthesis. *Biochemistry and Biophysics Reports* **18**, 100621, doi:https://doi.org/10.1016/j.bbrep.2019.100621 (2019).

37 Kwan, C. Y. & Achike, F. I. Tetrandrine and related bis-benzylisoquinoline alkaloids from medicinal herbs: cardiovascular effects and mechanisms of action. *Acta pharmacologica Sinica* **23**, 1057-1068 (2002).

38 Sakurai, Y. *et al.* Ebola virus. Two-pore channels control Ebola virus host cell entry and are drug targets for disease treatment. *Science* **347**, 995-998, doi:10.1126/science.1258758 (2015).

39 Onishi, E., Natori, K. & Yamazaki, S. The antiviral effect of phorbol ester and calcium ionophore A23187 is not mediated by interferons. *Journal of interferon research* **11**, 171-175, doi:10.1089/jir.1991.11.171 (1991).

40 Marois, I. *et al.* Inhibition of Influenza Virus Replication by Targeting Broad Host Cell Pathways. *PLOS ONE* **9**, e110631, doi:10.1371/journal.pone.0110631 (2014).

41 Geller, R., Taguwa, S. & Frydman, J. Broad action of Hsp90 as a host chaperone required for viral replication. *Biochimica et biophysica acta* **1823**, 698-706, doi:10.1016/j.bbamcr.2011.11.007 (2012).

42 Amraiz D, Z. N., Fatima M. Antiviral evaluation of an Hsp90 inhibitor, gedunin, against dengue virus. . *Trop J Pharm Res* **16**, 997-1004 (2017).

43 Vrijsen, R., Vanden Berghe, D. A., Vlietinck, A. J. & Boeyé, A. Lycorine: a eukaryotic termination inhibitor? *The Journal of biological chemistry* **261**, 505-507 (1986).

44 Yang, L. *et al.* Tandem mass tag-based quantitative proteomic analysis of lycorine treatment in highly pathogenic avian influenza H5N1 virus infection. *PeerJ* **7**, e7697-e7697, doi:10.7717/peerj.7697 (2019).

45 Ieven, M., van den Berghe, D. A. & Vlietinck, A. J. Plant antiviral agents. IV. Influence of lycorine on growth pattern of three animal viruses. *Planta medica* **49**, 109-114 (1983).

46 Szlávik, L. *et al.* Alkaloids from Leucojum vernum and antiretroviral activity of Amaryllidaceae alkaloids. *Planta medica* **70**, 871-873, doi:10.1055/s-2004-827239 (2004).

47 Li, S. Y. *et al.* Identification of natural compounds with antiviral activities against SARS-associated coronavirus. *Antiviral Res* **67**, 18-23, doi:10.1016/j.antiviral.2005.02.007 (2005).

48 Liu, J. *et al.* Lycorine reduces mortality of human enterovirus 71-infected mice by inhibiting virus replication. *Virology journal* **8**, 483, doi:10.1186/1743-422x-8-483 (2011).

49 Li, S., Liu, X., Chen, X. & Bi, L. Research Progress on Anti-Inflammatory Effects and Mechanisms of Alkaloids from Chinese Medical Herbs. *Evidence-Based Complementary and Alternative Medicine* **2020**, 1303524, doi:10.1155/2020/1303524 (2020).

50 Rajapakse, A. G., Ming, X. F., Carvas, J. M. & Yang, Z. The hexosamine biosynthesis inhibitor azaserine prevents endothelial inflammation and dysfunction under hyperglycemic condition through antioxidant effects. *American journal of physiology.*

Heart and circulatory physiology **296**, H815-822, doi:10.1152/ajpheart.00756.2008 (2009).

51 Botz, B. *et al.* Differential regulatory role of pituitary adenylate cyclase-activating polypeptide in the serum-transfer arthritis model. *Arthritis & rheumatology (Hoboken, N.J.)* **66**, 2739-2750, doi:10.1002/art.38772 (2014).

52 Sasaki, T. *et al.* Inhibitory effect of di- and tripeptidyl aldehydes on calpains and cathepsins. *Journal of enzyme inhibition* **3**, 195-201, doi:10.3109/14756369009035837 (1990).

53 Schneider, M. *et al.* Severe acute respiratory syndrome coronavirus replication is severely impaired by MG132 due to proteasome-independent inhibition of M-calpain. *J Virol* **86**, 10112-10122, doi:10.1128/jvi.01001-12 (2012).

54 Upla, P. *et al.* Calpain 1 and 2 are required for RNA replication of echovirus 1. *J Virol* **82**, 1581-1590, doi:10.1128/jvi.01375-07 (2008).

55 Zheng, K. *et al.* Calcium-signal facilitates herpes simplex virus type 1 nuclear transport through slingshot 1 and calpain-1 activation. *Virus research* **188**, 32-37, doi:10.1016/j.virusres.2014.03.016 (2014).

56 Ma, C. *et al.* Boceprevir, GC-376, and calpain inhibitors II, XII inhibit SARS-CoV-2 viral replication by targeting the viral main protease. *Cell research* **30**, 678-692, doi:10.1038/s41422-020-0356-z (2020).

57 Barnard, D. L. *et al.* Inhibition of severe acute respiratory syndrome-associated coronavirus (SARSCoV) by calpain inhibitors and beta-D-N4-hydroxycytidine. *Antiviral chemistry & chemotherapy* **15**, 15-22, doi:10.1177/095632020401500102 (2004).

58 Blanc, F. *et al.* Targeting host calpain proteases decreases influenza A virus infection. *American journal of physiology. Lung cellular and molecular physiology* **310**, L689-699, doi:10.1152/ajplung.00314.2015 (2016).

59 Li, X. *et al.* Over-expression of calpastatin inhibits calpain activation and attenuates myocardial dysfunction during endotoxaemia. *Cardiovascular research* **83**, 72-79, doi:10.1093/cvr/cvp100 (2009).

60 Supinski, G. S. & Callahan, L. A. Calpain activation contributes to endotoxin-induced diaphragmatic dysfunction. *American journal of respiratory cell and molecular biology* **42**, 80-87, doi:10.1165/rcmb.2008-0275OC (2010).

61 DeBiasi, R. L., Edelstein, C. L., Sherry, B. & Tyler, K. L. Calpain inhibition protects against virus-induced apoptotic myocardial injury. *J Virol* **75**, 351-361, doi:10.1128/jvi.75.1.351-361.2001 (2001).

62 Baker, J. D., Uhrich, R. L., Kraemer, G. C., Love, J. E. & Kraemer, B. C. A drug repurposing screen identifies hepatitis C antivirals as inhibitors of the SARS-CoV2 main protease. *PLOS ONE* **16**, e0245962, doi:10.1371/journal.pone.0245962 (2021).

63 Sugamata, R. *et al.* Leucomycin A3, a 16-membered macrolide antibiotic, inhibits influenza A virus infection and disease progression. *The Journal of antibiotics* **67**, 213-222, doi:10.1038/ja.2013.132 (2014).